



# Inkjet printed graphene-metal oxide miniaturised gas sensors

B-TH270-1

Author Name: Yungyu Song  
Supervisor: Dr. Tawfique Hasan

Date: 27<sup>th</sup> May 2020

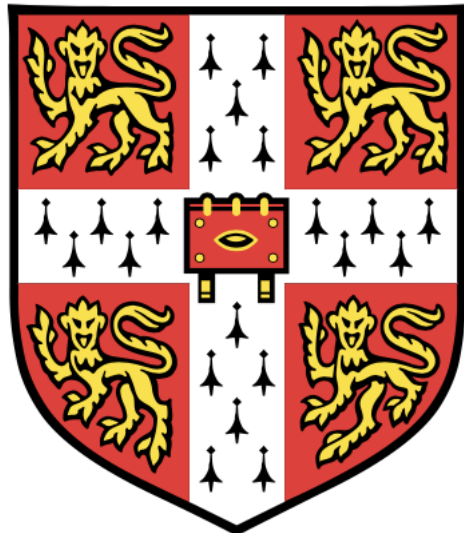
I hereby declare that, except where specifically indicated, the work submitted herein is my own original work.

Signed: \_\_\_\_\_

A handwritten signature in black ink, appearing to read "Yungyu Song".

Date: 27/05/20

# Inkjet Printed Graphene Metal Oxide Miniaturized Gas Sensors



**Yungyu Song**  
Department of Engineering  
University of Cambridge

May 2020

## Abstract

Chemiresistive gas sensors based on reduced graphene oxide (rGO)/metal oxide (MOx) composite are currently considered as the next generation sensing devices due to their advantages over the conventional MOx counterparts. The merits of using rGO/MOx composite derive from material properties of rGO and its interaction with MOx. In this report, theories on the sensor mechanism are discussed in depth, allowing identification of rGO/MOx sensors' properties as well as defects which require improvements.

After a thorough analysis of the background theory, different processes involved in rGO/MOx based gas sensors are studied. Three different metal oxides are used in this project: Cu<sub>2</sub>O, Co<sub>3</sub>O<sub>4</sub>, and CuCoO<sub>x</sub>, to synthesize rGO/MOX sensors via inkjet printing. The materials will each be used to describe the common experimental characteristics of 2D incorporated gas sensors and discuss possible methods to allow improvements in sensors' performance.

Characterisation and testing are first done on rGO/Cu<sub>2</sub>O sensors to portray archetypal rGO/MOx sensor traits. Different techniques such as SEM, sessile drop method are involved which are used to deepen the knowledge on the nanocomposite and the formulated ink. The sensor also undergoes testing to provide common sensor response to analytes.

The processes above allow identification of two major issues with gas sensing: inaccuracy from baseline drift and selectivity. An attempt at reducing the baseline drift was made via inputting pulse signals to rGO/Co<sub>3</sub>O<sub>4</sub> sensor, which was unsuccessful due to several constraints. On the other hand, selectivity improvement was achieved using PCA with classifiers using rGO/CuCoO<sub>x</sub> sensor, allowing distinction between similar responses to analytes in different humidity settings, up to an approximated accuracy of 75% which can be optimised. However, the data used for this analysis was created from assumptions and a pseudo-random data generator, due to Covid-19 disruptions

Overall, the project allows a deeper understanding on rGO/MOx gas sensors. Throughout the duration of the project, it was possible to explore different aspects of gas sensing technology, from the synthesis processes to performance optimization based on theoretical background developed from the project. Different data processing techniques were also explored, with selectivity improvements through use of PCA and classifiers. Finally, the report concludes with ideas and suggestions that could be used in future to further complete the research.

## **Acknowledgements**

The research was done at Hybrid Nanomaterials Engineering group at University of Cambridge. I am fortunate to have Dr. Tawfique Hasan as project supervisor, and I would like to express my most sincere gratitude to him not only for his continuous guidance and knowledge that he shared with me, but also for his encouragements. I would also like to thanks Dr. Luigi Occhipinti for his feedbacks on the project.

Additionally, I would like to appreciate the irreplaceable help and assistance from Mr. Osarenkhoe Uwuigbe throughout the project. I am very much indebted to his kind cooperation and advice I was able to receive during the entirety of my research.

I would also like to thank my girlfriend for providing me valuable support during this unprecedented times.

Finally, I am grateful to my family for their support and love. Without them this work would never have come into existence.

# Contents

<b>1</b>	<b>Introduction</b>	<b>3</b>
1.1	Background and Motivations . . . . .	3
1.2	Aims . . . . .	5
1.3	Report Structure . . . . .	5
<b>2</b>	<b>Gas Sensing Technology</b>	<b>6</b>
2.1	Electrically-Transduced Sensors . . . . .	6
2.1.1	Components of Electrically-Transduced Gas Sensors . . . . .	6
2.1.2	Sensing Mechanisms . . . . .	9
2.1.3	Sensor Performance Parameters . . . . .	11
2.1.4	Sensor Architectures . . . . .	12
2.2	Processing Sensing Data . . . . .	14
<b>3</b>	<b>Sensing Materials</b>	<b>15</b>
3.1	Metal Oxides (MO <sub>x</sub> ) . . . . .	15
3.2	Two Dimensional (2D) Materials and Their Incorporation with MO <sub>x</sub> for Gas Sensing . . . . .	16
<b>4</b>	<b>Sensor Fabrication and Characterisation</b>	<b>18</b>
4.1	Device Fabrication . . . . .	18
4.1.1	rGO/MO <sub>x</sub> Composite Ink Synthesis . . . . .	18
4.1.2	Printing . . . . .	19
4.2	Ink Characterisation . . . . .	20
4.2.1	SEM . . . . .	21
4.2.2	Rheology . . . . .	22
4.3	Initial Gas Sensing Result . . . . .	23
<b>5</b>	<b>Sensor Optimisation - Baseline Drift</b>	<b>25</b>
5.1	Background Theory . . . . .	25

5.2	Pulse Exposure Results . . . . .	26
5.3	Discussion . . . . .	29
<b>6</b>	<b>Sensor Optimisation - Principal Component Analysis (PCA)</b>	<b>32</b>
6.1	Background Theory - PCA . . . . .	32
6.2	Background Theory - Classifiers . . . . .	34
6.3	Application of PCA on Gas Sensing Data . . . . .	35
6.4	PCA Results . . . . .	36
6.5	Discussion . . . . .	39
<b>7</b>	<b>Conclusion</b>	<b>42</b>
7.1	Main Findings . . . . .	42
7.2	Ideas for the future . . . . .	42
	<b>References</b>	<b>43</b>
<b>A</b>	<b>Codes for PCA/Classifiers and Pseudo-Random Data Generator</b>	<b>48</b>
<b>B</b>	<b>Risk Assessment Retrospective</b>	<b>49</b>
<b>C</b>	<b>Covid-19 Disruption</b>	<b>50</b>

# Chapter 1

## Introduction

### 1.1 Background and Motivations

Ever since the beginning of industrial revolution from the late 18<sup>th</sup> century, gas detection technology became essential with the discovery of harmful gases causing adverse effects on human health. This naturally lead to the development of the first generation gas sensor for miners, the Davy lamp, in 1815. While the lamp was successfully able to detect hazards, it proved to be unreliable due to several elements, such as surrounding airflow and its structural integrity [1].

The gas detection technology then saw significant improvement in the second half of the 20<sup>th</sup> century with the introduction of electronic technologies. Different types of gas sensors with various sensing mechanisms were created, allowing improved performance, reliability, portability, and cost [2][3]. Such advancements allowed the technology to expand its use beyond mining industry and be incorporated into a wider range of systems. In the recent years, the gas detection technology is ubiquitous, with its use in industries, manufacturing, healthcare, and environmental protection (see figure 1.1).

Of the various types of sensors developed, electrically-transduced devices are currently dominating the market, particularly chemiresistive sensors based on metal oxide (MOx) due to their simple architecture, relatively high sensitivity [4], and potential for device integration into a more complex system. However, MOx sensors present significant disadvantages such as high power consumption, low selectivity, poor control during manufacturing process, slow response/recovery speed at low temperature, and other performance issues which require improvements [5][6].

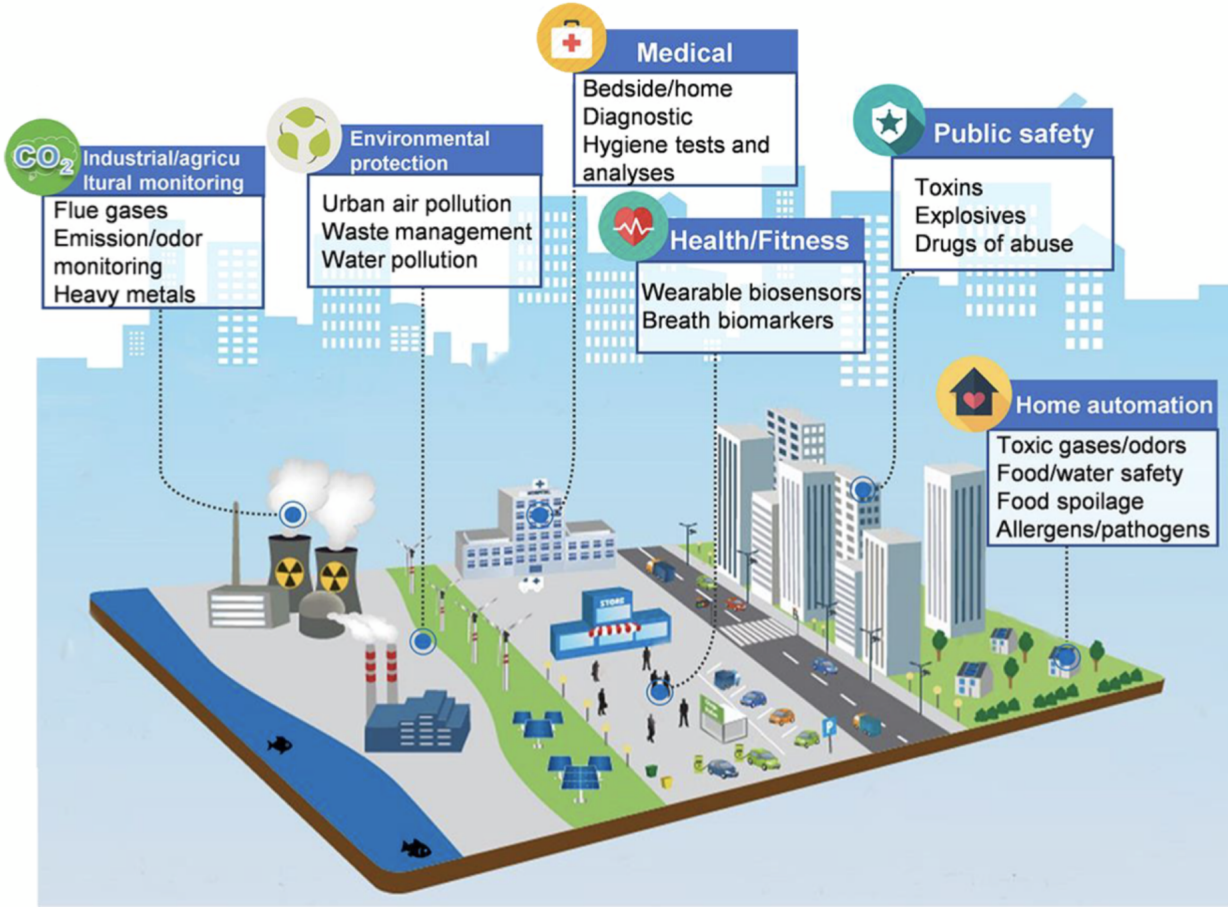


Figure 1.1: Illustration showing uses of gas sensing technology in daily life [7]

Most limitations of gas sensors listed above derive from the electrochemical properties of the sensing material. Therefore, graphene and other two dimensional materials, such as GO/rGO(Graphene Oxide/reduced Graphene Oxide), BP (Black Phosphorus), and transition metal dichalcogenides, are currently considered as candidates for sensing materials in gas sensors, due to their intrinsic properties allowing improved gas sensing performance. Such characteristics include higher sensitivity from large surface-to-volume ratio and conductivity from their bandgaps, encompassing metals, semi-metals, insulators, and semiconductors [8]-[10]. Moreover, the use of 2D materials allows a more controlled deposition in various methods such as inkjet printing, facilitating device fabrication process. These traits of 2D materials can be exploited through their integration into the traditional MOx gas sensors, allowing remarkable advances to be made and enhancing their performances. However, the continued use of MOx in the device and the intrinsic features of chemiresistive sensors lead to similar shortcomings in the novel sensors [7] which remain issues to be addressed in the current researches.

## 1.2 Aims

The goal of the project is to first use reduced graphene oxide as the 2D material to be integrated into MO<sub>x</sub>, to develop a functioning rGO/MO<sub>x</sub> composite based gas sensor. This will be achieved through synthesis of rGO/MO<sub>x</sub> composite using hydrothermal process to allow complete combination of the two materials. Different gas sensors will be made using various MO<sub>x</sub> materials: Cu<sub>2</sub>O, Co<sub>3</sub>O<sub>4</sub>, and CuCoO<sub>x</sub> are chosen for the purpose of this project. To allow a uniform and repeatable device fabrication, inkjet printing method will be used. The target analytes of the gas sensors for this project are potentially deleterious gases such as NO<sub>2</sub>, NH<sub>3</sub>, and CO<sub>2</sub>.

Once the device fabrication process is complete, different methods for sensors' performance optimisation are explored. Firstly, an operating regime for rGO/MO<sub>x</sub> gas sensor will be designed to attempt reduction of baseline drift which lead to inaccuracies in the sensor readings. This will be achieved by running the sensor at different voltage cycles, which include variation of DC voltage level and voltage pulses.

The selectivity issues of the sensor, specifically from the presence of humidity, will then be tackled through use of PCA (Principal Component Analysis) using python. The developed gas sensor will undergo gas cycles in both humid and dry ambient conditions, and their data will be juxtaposed. Classifiers will be used in this process to categorise the results. This will provide a visual output showing the effect of humidity on gas sensing behaviour and potentially achieve data independence from the error source.

## 1.3 Report Structure

The report structure will follow the progresses I was able to make throughout the duration of my fourth year project. The two following chapters will cover the theoretical background behind the project, explaining how the gas sensor operates and provide details on the materials used for the purpose of the experiments conducted throughout the project. Chapter 4 will describe the steps behind the device fabrication, as well as different characterisation and gas sensing tests on rGO/MO<sub>x</sub> composite inks, providing deeper understanding on the gas sensing devices. Chapter 5 and 6 will then describe the progresses made in device optimisation in terms of its baseline drift removal and selectivity, based on different sensor measurements. Finally, the last chapter will include the conclusions and ideas for future research.

# Chapter 2

## Gas Sensing Technology

### 2.1 Electrically-Transduced Sensors

Chemical sensors are classified with the nature/phase of the targeted analytes: gas, liquid, and solid particulate sensors [11]. They can be further subdivided through their principles of transduction, into either optical, electrochemical, thermometric, or gravimetric sensors [3]. Of the various types of sensors, the project will focus on electrically-transduced gas sensors. This chapter will offer an insight on how electrically-transduced sensors work: details on their different components, mechanisms, parameters, and architectures will be provided.

#### 2.1.1 Components of Electrically-Transduced Gas Sensors

Electrically-transduced gas sensors consists of two main elements: a recognition component and a transducer (see figure 2.1). The recognition element interacts either covalently or non-covalently with the target analyte and allows the determination of their chemical parameters (concentration, identity of the analyte). This identification then leads to change in one or more physical properties: conductivity ( $\sigma$ ), work function ( $\varphi$ ), and permittivity ( $\varepsilon$ ) [12].

Following the recognition, the changes in the parameters above are converted into electric signals, as the name electrically-transduced indicates. The property changes are converted into quantifiable electrical signal, such as current (I), capacitance (C), resistance/impedance (R/Z), voltage (V), or electrical potential (E). The transduced signals can then be further processed and used to determine the concentration of reactants.

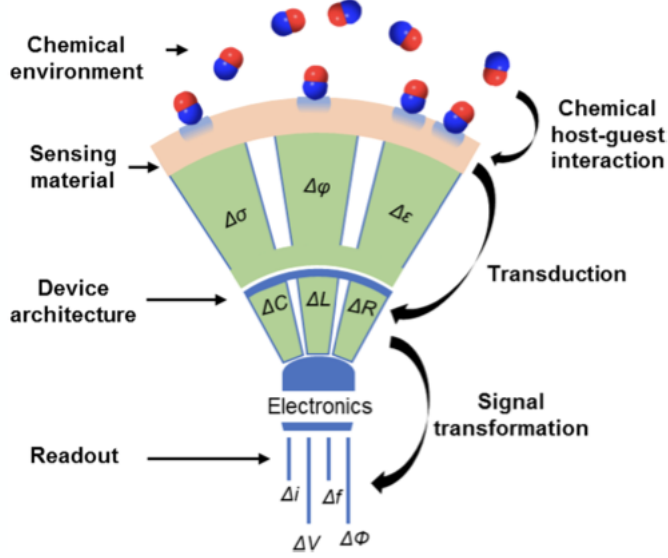


Figure 2.1: Logical structure of a chemical sensor, frequency ( $f$ ) and phase ( $\Phi$ ) can also be used for transduction [12]

From above, the characteristics required for the components of electrically-transduced gas sensors can be specified.

### Recognition Component

Firstly, it is imperative that the sensing material in the recognition component is able to interact with surrounding environments to detect the relevant analytes' presence. This is achieved by presence of active sites which allow analyte-sensing material interaction. These sites can be either inherent or added through post-synthetic modifications [7].

Another key aspect is the recognition component's ability to convert detection of analytes into quantifiable changes in physical properties, notably its conductivity, work function, and permittivity. The conductivity ( $\sigma$ ) property obeys equation 2.1 [13].

$$\sigma = e(\mu_e n_e + \mu_h n_h) \quad (2.1)$$

The equation shows that the conductivity is dependent of electron/hole mobility (charge carrier mobility,  $\mu_e/\mu_h$ ) and its respective density ( $n_e/n_h$ ). The charge carrier density is a material property, which may be altered through processes such as doping. This variable is further related to the bandgap of the material and the surrounding temperature, as shown in the equation 2.2 [14].

$$n = CT^{\frac{3}{2}} e^{\frac{-E_g}{2k_B T}} \quad (2.2)$$

Bandgap energy ( $E_g$ ) is the difference between the conduction band ( $E_c$ ) and valence band energy values ( $E_v$ ).  $n$  corresponds to either the electron or hole density,  $C$  to a constant, and  $T$  to temperature.

Mobility is dependent of drift velocity ( $v_d$ ) and electric field ( $\mathcal{E}$ ) and is related via the following equation.

$$\mu = \frac{v_d}{\mathcal{E}} \quad (2.3)$$

$\mu$  corresponds to the electron or hole mobility.

Work function is another relevant property for the recognition element. The parameter ( $W$ ) measures the amount of energy required to move an electron from Fermi energy level ( $E_f$ ), to the vacuum level ( $E_{vac}$ ) [15].

$$W = -e\psi - E_F \quad (2.4)$$

$\psi$  corresponds to the electrostatic potential.  $W$  therefore has a dependence on potential applied to the material. This leads to equation 2.5, where work function is linked with external potential (V) [16].

$$\psi = V - \frac{W}{e} \quad (2.5)$$

Finally, the permittivity can be used for recognition. Permittivity corresponds to a measure of how easily electromagnetic radiation can travel through a material [7]. It is a function of vacuum permittivity ( $\epsilon_0$ ) and relative static permittivity ( $\epsilon_r$ ) which is related to electric susceptibility ( $\chi$ ) [17].

$$\epsilon = \epsilon_0 \epsilon_r = (1 + \chi) \epsilon_0 \quad (2.6)$$

The three parameters discussed above directly impact the electrical changes observed. The relevant analytes may modify one or more of the listed properties, and the changes are then passed through a transducer which converts them to observable electric signals.

## Transducer

The purpose of the transducer is to convert the physical changes detected by the recognition element into electric signals. This requires integration of the recognition element into an electronic device. Different types of transducers exists for various architectures of gas sensors, the information for which is detailed later for chemiresistive gas sensors.

## 2.1.2 Sensing Mechanisms

Similarly to the gas sensor structure, it is possible to explain the underlying principles behind gas sensing in two different sections: the recognition component and the transducer. Similarly, this section will explain the sensing mechanisms of the gas sensor components: the analyte-sensing material interaction and transduction mechanisms.

### Mechanisms of Analyte-Sensing Material Interactions

As described previously, the interaction between the sensing material and the analyte occurs either covalently or non-covalently. Covalent interactions forms covalent bonds, which occurs as electrons are shared between the sensing material and the analytes. While this provides high selectivity and sensitivity, the process leads to an irreversible response due to the bonds' strength [7]. On the other hand, non-covalent interactions arise from van der Waals forces, hydrogen bonding, coordination, and  $\pi$ - $\pi$  interactions [7]. These are weaker than the covalent interactions, but allow full/partial reversibility. The interactions are determined by the chemical structure/composition of the materials involved, enabling either full or partial selectivity to be achieved in the gas sensors [12]. The characteristics are usually expressed as active sites for analyte-sensing material interactions, and can be introduced through manipulation of the material such as introduction of defects and doping.

### Mechanisms of Transduction

The transduction mechanism is the second core mechanism of electrically-transduced gas sensors. The transfer of physical changes to electrical signals can be explained through three methods: modulation of doping effect, modulation of Schottky barrier, and finally formation of dipole and interfacial layer.

#### *Modulation of the Doping Level*

During the interaction of an analyte with the material, the distance between the target molecule and sensory material becomes close enough for electron transfer to occur [18]. Analyte can then act either as an electron donor (n-type dopant) or an electron receiver (p-type dopant), as shown in figure 2.2. As charge transfer occurs between the materials, change in charge carrier density occurs. This leads to modification of the sensing material's conductivity, the degree of which depends on the concentration of the target analyte.

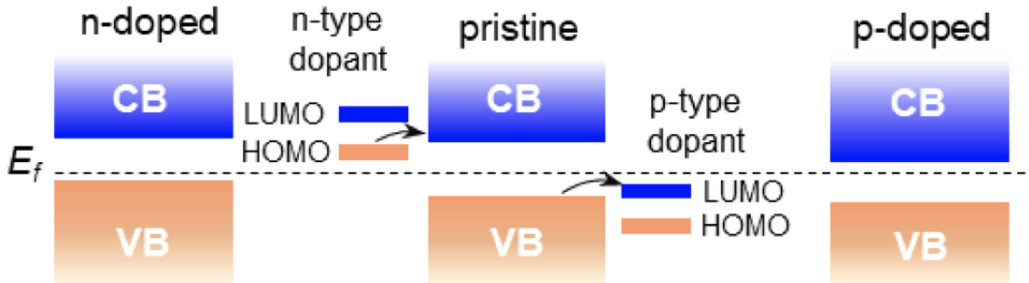


Figure 2.2: Scheme showing n- and p-type doping of a semiconductor. VB corresponds to valence band, CB to conduction band, HOMO to highest occupied molecular orbital, and LUMO to lowest unoccupied molecular orbital [19]

### *Modulation of the Schottky Barrier*

For a system where metal-semiconductor junction are involved, the two interact by forming a potential barrier due to the discrepancies in the work function (see figure 2.3). This potential barrier, depending on the direction of charge flow and bias, may prevent charge flow to occur across the materials. However, as interaction of the sensing material with analyte takes place, modulation of the doping level (explained previously) can lead to an alteration in the Fermi level and the work function. The changes are then translated into modifications in potential barrier which leads to conductivity variation in the sensing material.

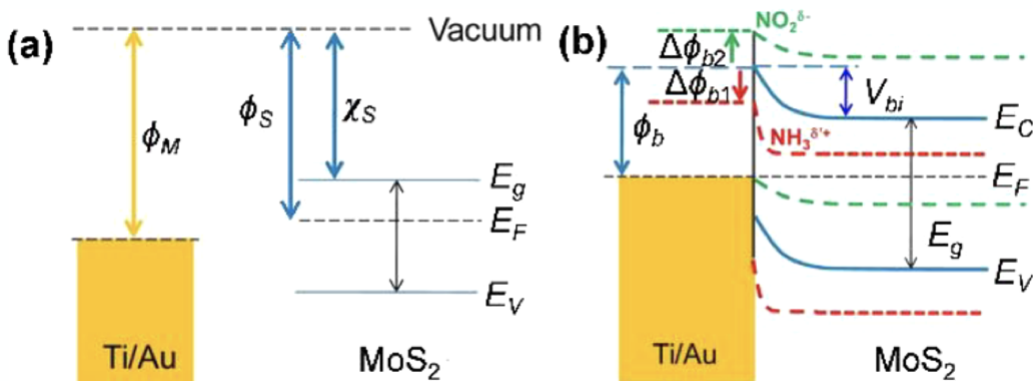


Figure 2.3: (a) Energy diagram of the Ti/Au and MoS<sub>2</sub> before contact.  $\Phi_M$  and  $\Phi_m$  are work functions of the metal and semiconductor, respectively, and  $\chi_s$  is the electron affinity of the semiconductor.  $E_C$ ,  $E_F$ , and  $E_V$  represent the energy level of conduction band and Valence band, and Fermi level, respectively.  $E_g$  is the band gap, difference between  $E_C$  and  $E_V$ . (b) Band realignment and energy diagram of the Ti/Au and MoS<sub>2</sub> after contact and the formation of Schottky barrier. Blue, green and red lines indicate the energy band of the pristine MoS<sub>2</sub> (solid blue), after exposure to NO<sub>2</sub> (dashed green), and after exposure to NH<sub>3</sub>, (dashed red), respectively.  $V_{bi}$  is the built-in voltage [20]

### Formation of Dipole and Interfacial Layer

The final transduction mechanism can be explained considering two forms of interaction between materials. Firstly, dipole layer formation occurs from polarisation or ionisation of the analytes at the sensing material surface [21] (see figure 2.4.(a)). This signifies that the analyte distributes charge carriers which lowers the barrier in material/metal junction of the sensor. This thus provides an output signal dependent on the concentration of absorbed analytes.

On the other hand, interfacial layer may be formed where analytes forms an excess charge states between material/metal junction, leading to modulation of the Schottky barrier height (see figure 2.4.(b)). From previous explanations, this causes changes in conduction. It must also be noted that the interfacial layer must be capable of supporting charge carrier flow, and must therefore have a thickness less than  $50\text{\AA}$  [22][23].

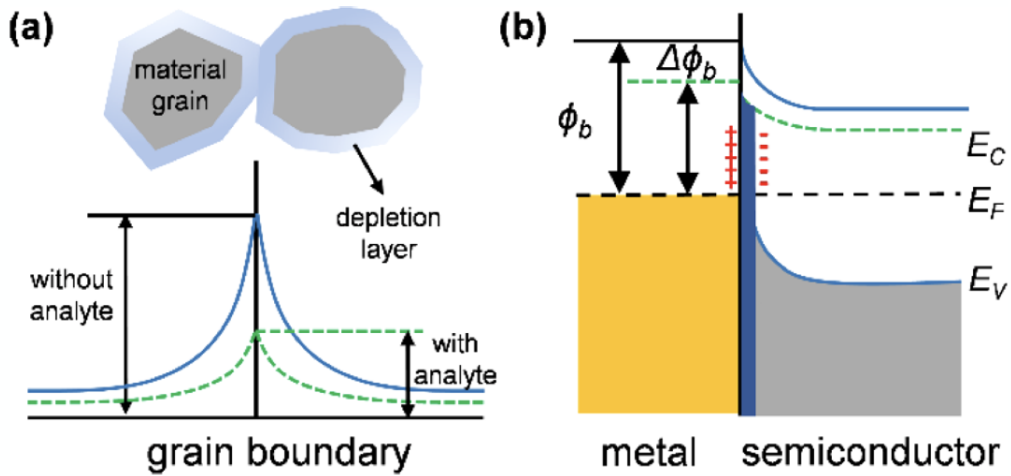


Figure 2.4: Band diagrams of a metal/semiconductor Schottky contact (a) without and (b) with formation of an interfacial layer after the analyte absorption [24][25]

### 2.1.3 Sensor Performance Parameters

In order to evaluate different sensors and determine their characteristics, universal performance parameters must be implemented. The report will focus on improving two parameters in particular: drift and selectivity. Drift is the slow, non-random change of analytical signal with time while the concentration of measured analyte remains constant [26][27]. This is caused by several imperfections, such as electrochemical, mechanical instability, material degradation, and poor performance, with slow response/recovery time of the sensor. The parameter can be observed by plotting the sensor response (shown later in figure 2.6).

Selectivity is another important parameter, which describes the extent to which an analytical method can discriminate between analytes of interest in multicomponent mixtures, without interference from other components [28][29]. The parameter can be quantified by comparing sensor response to different types of analytes, while ensuring that the experimental conditions are kept uniform for all analytes.

#### 2.1.4 Sensor Architectures

Electrically-transduced sensors have different architectures which generally fall into the following categories: chemiresistive sensors, chemical diode, FET, chemical capacitor, and electrochemical sensor [30]. As explained briefly in the previous section, the current gas sensor market is dominated by chemiresistive gas sensors based on MOx due to its simple architecture, low cost of production, and its compatibility with DC circuits. Hence, this section will focus on the description of chemiresistive sensors and detail the different performance parameters involved in the device.

##### Chemiresistive Gas Sensors

Chemiresistive gas sensors have extremely simple base structure, consisting of two conducting electrodes connected to a sensing material which is chemiresistive. The most popular type of material for this usage is MOx (metal oxides), and the material is deposited on a dielectric substrate (see figure 2.5). Exposure of the sensitive material to the analytes will result in physical changes which follow either one or several of the recognition mechanisms described above, altering the material conductance. For chemiresistive gas sensors, this change is manifested by modification in the resistance value of the component. The value can be described with two components, as shown below.

$$R = R_{\text{mat}} + R_{\text{contact}} \quad (2.7)$$

$R$  corresponds to the total resistance,  $R_{\text{mat}}$  to the resistance of the sensing material, and  $R_{\text{contact}}$  to the resistance originating from the metal electrode/sensing material junctions and junctions of the material grains [7].

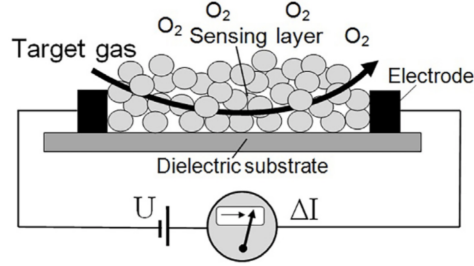


Figure 2.5: Illustration of an electrochemical gas sensor and its structure [31]

The change in resistance is directly correlated to the sensor's sensitivity,  $S$ . It is one of the sensor's performance parameter and can be described with equation 2.8 and 2.9.  $R_0$  is the base sensor resistance and  $R_{analyte}$  is the resistance of the sensor after interaction with the analyte.

$$S = \frac{\Delta R}{R_0} = \frac{R_{analyte} - R_0}{R_0} \times 100\% \quad (2.8)$$

$$S = \frac{\Delta I}{I_0} = \frac{I_{analyte} - I_0}{I_0} \times 100\% \quad (2.9)$$

The sensor performance can be characterised through other features. Figure 2.6 illustrates a typical chemiresistive sensor's response with performance parameters than can be applied for the sensor architecture.

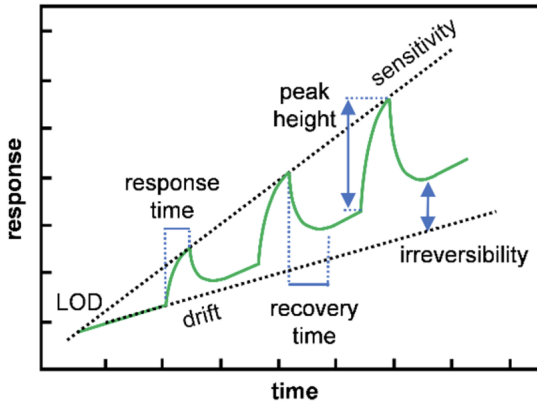


Figure 2.6: Graphical representation of selected performance parameters in a device successively exposed to increasing concentrations of analyte. LOD corresponds to limit of detection [32]

It is important to note the presence of drift from the graph, with the response curve shifting upwards with each exposure to analyte. This issue will be addressed in the following pages along with selectivity problems of common chemiresistive sensors.

## 2.2 Processing Sensing Data

Once raw data collection is achieved, it is possible to apply processing techniques to deepen the understanding on how the sensor performs. The method of choice for the project is the application of PCA (principal component analysis) on the data for dimensionality reduction.

To achieve this technique, several parameters are taken from gas sensing data. The data must ideally be parameters which provide an adequate measure of the sensors' performance. These include variables such as maximum sensor response, response time, recovery time, curve area, and so on. To then provide visual data on a 2 or 3 dimensional scale, the dimension reduction of the data must be completed, through PCA. The technique is defined as an orthogonal linear transformation, which converts the data into a new coordinate system, such that the greatest variance by some scalar projection of the data comes to lie on the first coordinate (the first principal component, PC1), the second greatest variance on the second coordinate (PC2), and so on [33]. This technique additionally provides information on the importance of the principal component, by providing a percentage value which expresses how much variation each PC (principal component) accounts for. An example of the technique applied on gas sensing data is provided in figure 2.7.

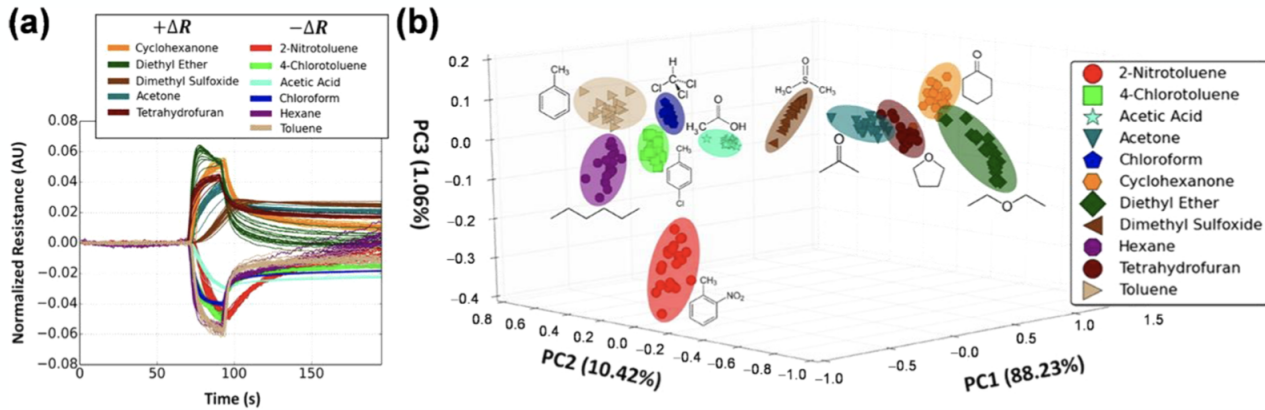


Figure 2.7: (a) Normalized sensor response to a chemically diverse set of compounds and (b) corresponding PCA transform [34]

The PCA result shown above provides an example of how the dimensionality reduction technique outputs a clear visual data, allowing clear distinction from raw data showing seemingly similar responses. This can then be used to classify the responses in order to improve the selectivity of the device. This will be explained in more detail in chapter 6.

# Chapter 3

## Sensing Materials

### 3.1 Metal Oxides (MOx)

As described previously, the most common sensing material in chemiresistive gas sensors is MOx. MOx possesses pre-absorbed oxygen species on their surfaces acting as active sites for gas interaction. As MOx presents oxygen-rich surfaces, it is sensitive particularly towards reducing and oxidising gases [7]. This can be modified using material processing techniques such as doping and introduction of extrinsic chemical species. The gas sensing behaviour of MOx can be further elaborated through figure 3.1. From the figure, MOx first functions as a receptor with presence of surface oxygen groups which are the active sites [31]. MOx then shows a transducer behaviour where its depletion region thickness is modified from redox reactions (see figure 3.1), inducing changes in Schottky barrier of the material and thus its conductance [35].

While MOx presents benefits such as its structural simplicity and low cost of production, its weaknesses must also be highlighted. Firstly, MOx incurs high power consumption as it requires a heating element to operate as a sensing material. MOx is by nature a semiconductor, and thus high thermal energy is required to allow the device to conduct and operate as a sensor through redox interactions with target gases. The need for a heating element in the sensor causes high power consumption in traditional MOx sensors as a result [36]. Moreover, MOx generally suffer from slow response and recovery times [7], leading to a baseline drift (see figure 2.6). Additionally, MOx growth on a dielectric layer is problematic, due to difficulty in controlling grain size of the MOx to provide a uniform structure and morphology, leading to device instability [37]. The disadvantage is highlighted especially when creating nanostructures using MOx, as the issue renders nanoscale manipulation to be extremely challenging. Finally, the MOx based gas sensors have significant problems with the

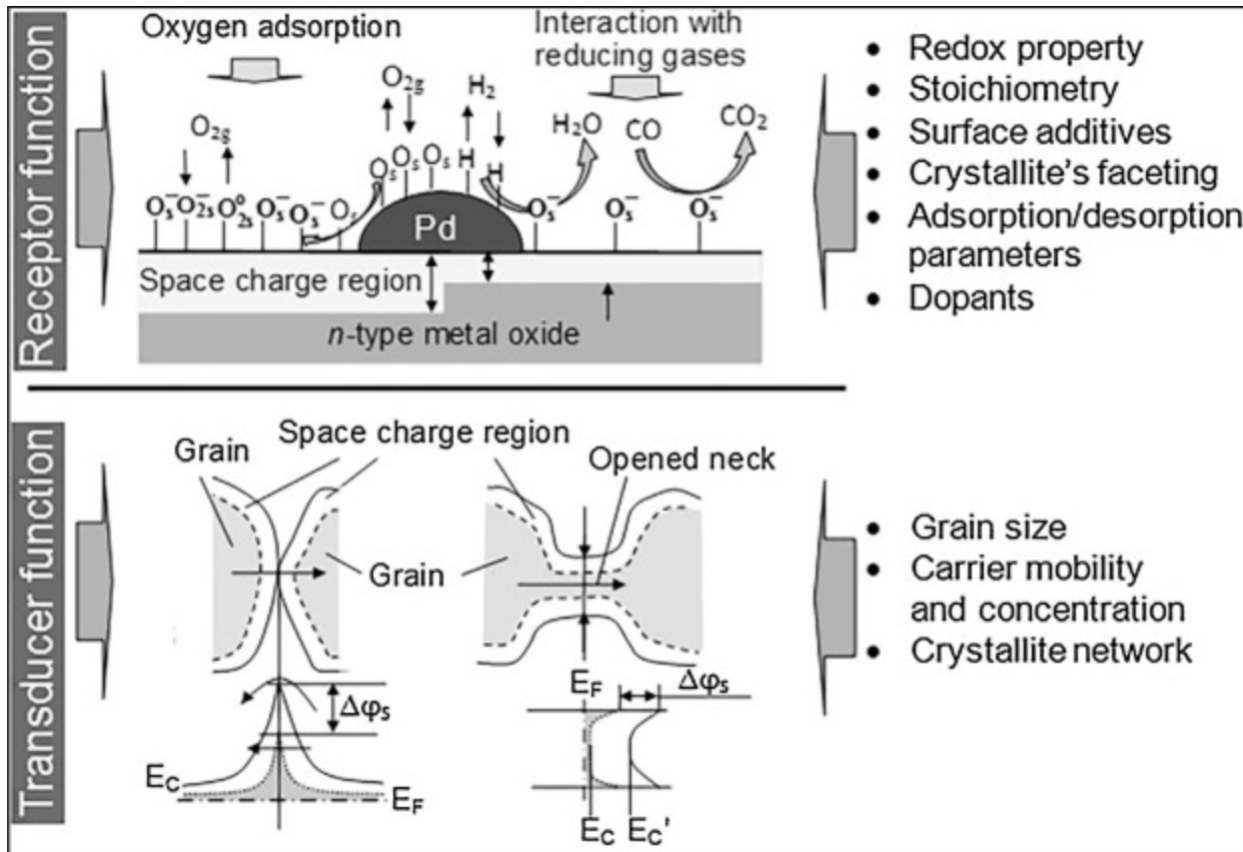


Figure 3.1: Receptor and transducer functions as well as their physicochemical and material properties of metal oxide semiconductor gas sensor [31]

device selectivity, due to highly reactive nature of surface oxygen groups. A notable example would be the unwanted sensitivity of MOx to humidity, where its presence alters the reading output.

### 3.2 Two Dimensional (2D) Materials and Their Incorporation with MOx for Gas Sensing

As detailed previously, there are several intrinsic problems with the material which must be addressed for device optimisation. Hence, several researches are focused on finding novel materials allowing optimised sensing behaviours. The project focuses on gas sensors based on incorporation of two materials, rGO (reduced graphene oxide), a 2D material, with various MOxs, more specifically copper (I) oxide ( $Cu_2O$ ), cobalt (II, III) oxide ( $Co_3O_4$ ), and copper-cobalt oxide ( $CuCoO_x$ ).

The use of rGO and its incorporation into MOx presents several advantages for gas sensing. Firstly, rGO is a 2D material which possesses by nature a large surface-to-volume ratio, leading to high sensitivity. Additionally, rGO is a conductor, thus presenting a more favorable electronic property than MOx [38]. The rGO properties therefore allows the sensor to operate without the need of a heat source, reducing power consumption as heat source is no longer needed for the sensor operation. Moreover, rGO provides enhanced solubility over other 2D materials such as graphene due to the presence of -OH functional groups in its structure. This allows the rGO/MOx composite to be created as an ink for inkjet printing, which addresses the manufacturing issues raised by MOx. Additionally, rGO can be chemically modified such as the amalgamation of high energy absorption sites which can further enhance sensor sensitivity, showing its versatility [39]. Finally, the composite operates similarly to conventional chemiresistive sensor, with similar sensing mechanisms as explained previously. This enables the device to retain its simple structure. However, the issue of baseline drift exists especially in room temperature conditions, as the disparity in absorption and desorption speed remains. Selectivity also persists, especially in humid conditions. This is aggravated by incorporating rGO, due to its functional groups and defects being reactive to water [7].

It is now possible to explain the MOx choices. Firstly, Cu<sub>2</sub>O is selected as the material was confirmed to be sensitive to one of the target analytes, NO<sub>2</sub>. Sow and co-works confirmed that immobilized Cu<sub>2</sub>O nanowires on rGO sheets showed higher response to NO<sub>2</sub> than that of rGO or Cu<sub>2</sub>O nanowires alone [40]. Hence, rGO/Cu<sub>2</sub>O composite will be used as a training material to understand the behaviour of rGO/MOx composites based chemiresistive gas sensors towards oxidising gases. Co<sub>3</sub>O<sub>4</sub> is then chosen as another material, now for sensor optimisation through baseline removal. Similarly to rGO/Cu<sub>2</sub>O, rGO/Co<sub>3</sub>O<sub>4</sub> is a single metal-oxide based nanocomposite with appropriate architecture for prototyping. Additionally, the material has relatively fewer research on its gas sensing performance in comparison to other nanocomposites. CuCoO<sub>x</sub> is the final material of choice in the experiment, for sensor optimisation through PCA. In contrast with previous materials, the CuCoO<sub>x</sub> contains two different metals, copper and cobalt. Such configuration is chosen as the presence of different oxides will introduce additional heterojunctions to be formed due to interaction between the metal oxides. This signifies that band bending will be more prominent for these devices as a result, leading to a more pronounced sensor response to different analytes (see section 2.1.2). Additionally, the use of the material is expected to shed light on how a multi-metal oxides material integrated with rGO will behave as a gas sensor, as there are currently very few studies on such materials for gas sensing applications.

# Chapter 4

## Sensor Fabrication and Characterisation

### 4.1 Device Fabrication

The device fabrication process can be divided into two large steps, the synthesis of rGO/MOx compound ink, and the printing process where both the electrodes and the sensing material layer will be inkjet printed on a dielectric substrate.

#### 4.1.1 rGO/MOx Composite Ink Synthesis

The ink synthesis process requires rGO/MOx composite to be formed through hydrothermal process, which involves application of pressure and heat to allow MOx growth on rGO flakes. This allows a more uniform and stable material property in comparison to simple rGO and MOx mixture. The synthesis process is common to all sensors involved in the project, and generally follows 3 steps, involving 1) solution preparation, 2) hydrothermal process, 3) post-processing for ink synthesis.

Firstly, GO (graphene oxide) solution is prepared by mixing GO powder with DI water as a solvent. This procedure is done in tandem with the preparation of MOx solution, where adequate MOx is mixed with DI water. Controlling the amount of GO and MOx is critical during this process, as failure to do so can result in undesirable electronic properties, such as excessive resistance value due to overabundance of MOx in the sensing material. Both solutions are then stirred thoroughly using a sonicator, and are mixed to be sonicated once again. Sonication not only allows a uniform mixture to be formed, but also breaks down GO into thin layers on which MOx will grow later on. Surfactant is then added, and the resultant

solution is sonicated again. Surfactant is included during this process to keep the GO layers separated from each other, preventing them from lumping and forming a cluster which can hinder MOx growth.

Hydrothermal process then takes place to allow MOx growth on rGO flakes, which is formed from reduction of GO using thermal energy [46]. This reduction is crucial as it transforms GO, an insulating material (due to abundance of  $sp^3$  C-C bonds [7]) into conducting rGO. Additionally, the temperature, pressure, and duration of the hydrothermal process is extremely important, as these parameters control the growth of MOx on rGO flakes, thereby manipulating the chemiresistive properties of the sensing material.

Once the hydrothermal process is complete, the binding agents in the resultant solution are removed via vacuum filtration. This finally yields solid rGO/MOx composite, which is mixed with IPA/Butan-2-ol at a 9:1 ratio to form a binder-free rGO/MOx ink, ready for inkjet printing. Some solid rGO/MOx can be extracted to undergo material characterisation such as SEM (scanning electron microscopy). The description for synthesis processes of the 3 types of inks used in the project,  $Cu_2O$ ,  $Co_3O_4$ , and  $CuCoO_x$ , is provided below in a tabular form.

Composite	MOx source	Surfactant	Hydrothermal process duration
$Cu_2O$	$Cu(NO_3)_2 \cdot H_2O$	$NaOH(aq)$	$60^\circ C$ for 2 hours
$Co_3O_4$	$Co(NO_3)_2 \cdot H_2O$	$NH_3(aq)$	$180^\circ C$ for 8 hours
$CuCoO_x$	$Cu(NO_3)_2 \cdot H_2O$ & $Co(NO_3)_2 \cdot H_2O$	$NH_3(aq)$	$180^\circ C$ for 8 hours

Table 4.1: Synthesis processes of  $Cu_2O$ ,  $Co_3O_4$ , and  $CuCoO_x$

#### 4.1.2 Printing

Following the ink synthesis, gas sensors can be fabricated using inkjet printing. The sensor will adapt the form of a typical chemiresistive sensor, hence the first step is printing sensor electrodes onto a dielectric substrate. Commercial silver nanoparticle ink is used to print the electrodes on a polymer sheet, which are arranged in an IDE (interdigitated electrode) structure (see figure 4.1). This structure allows both a more efficient fabrication process and a larger area of contact between the electrode and the sensing material, leading to increased

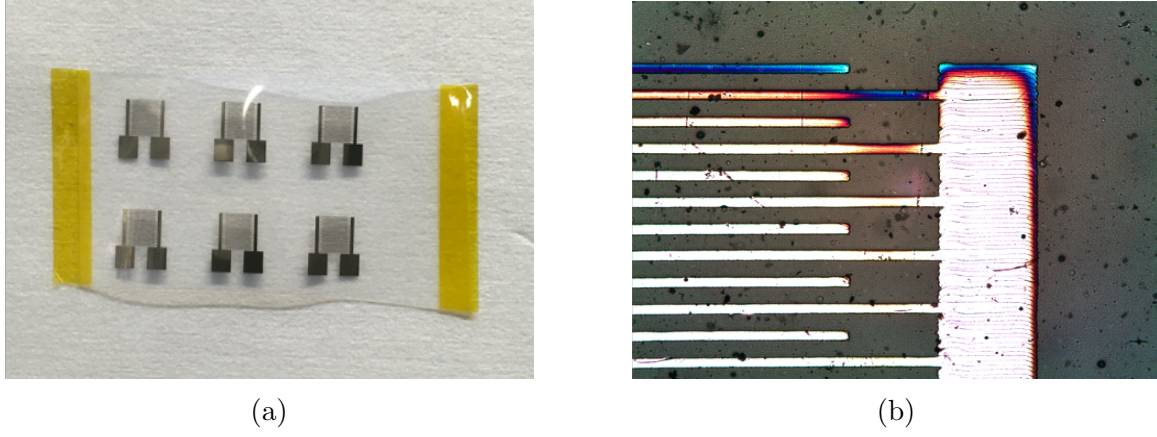


Figure 4.1: Ag based IDE (a) Macroscopic (b) Microscopic

sensor sensitivity [41][42]. The electrode is set to have a finger width of  $31.1\mu\text{m}$  and spacing of  $49.3\mu\text{m}$ . Both the IDE dimensions and material choice correspond to the standard configuration used in the lab group, and are chosen to allow sensor performance comparison as they are both variables which can modify gas sensor performance.

It must be noted that the IDE are configured such that conduction does not occur between the electrodes. Thus, the following step is to print the rGO/MOx ink on the interdigitated area of the sensor, where the newly printed layer acts as a sensing material and forms a conductive path. The sensor can then simply be tested using a multimeter to ensure the ink allows conduction: experimentally, it was found that the sensor shows a resistance value that ranges from several  $\text{k}\Omega$  to hundreds of  $\text{M}\Omega$ , depending on rGO/MOx property as well as the number of sensing material layers printed on the electrodes. Additionally, the sensor must be heated to evaporate the solvent on the ink to accurately measure its property. This thereby results in the formation a rGO/MOx chemiresistive gas sensor, and can be immediately tested.

## 4.2 Ink Characterisation

Once the sensor fabrication is completed by following the procedures detailed in the previous sections, it is possible to undergo different characterisation tests to analyse rGO/MOx inks to provide a deeper understanding on how the sensor functions, such as analyte-sensing material interactions.

#### 4.2.1 SEM

SEM, or scanning electron microscopy, allows direct observation of the ink and its nanocomposites. The technique reveals the surface topography of the sample, which enables the user to gain information on the sample structure and composition, providing further understanding on ink properties. The images are provided as follows.

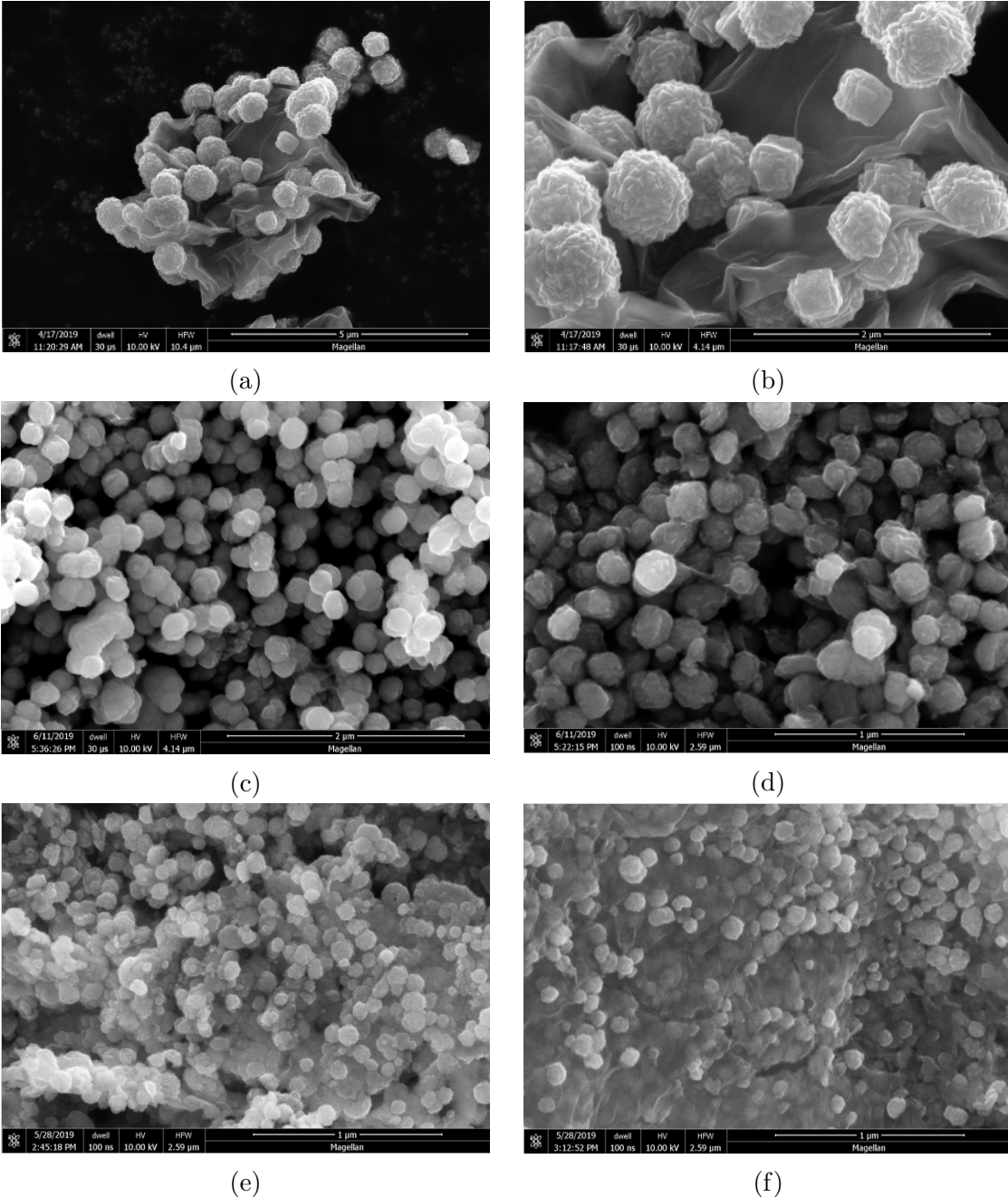


Figure 4.2: SEM images for three rGO/MOx nanocomposites: (a)&(b) rGO/Cu<sub>2</sub>O, (c)&(d) rGO/Co<sub>3</sub>O<sub>4</sub>, and (e)&(f) rGO/CuCoO<sub>x</sub>

From the results of the microscopy, it is possible to discern noticeable characteristics of rGO/MOx nanocomposites. Figures 4.2.(a) and (b) provide the optimal image: the images clearly show the presence of nanospheres, which corresponds to Cu<sub>2</sub>O on a thin and smooth surface, which is the rGO flake. A rGO/MOx nanocomposite is thus created, with both MOx and rGO acting as active sites for sensing material-analyte interactions to occur. Figures 4.2.(c) and (d), on the other hand, shows a heavier presence of MOx nanospheres over rGO flakes. This can be attributed to different factors, such as increased concentration of MOx during synthesis process, faster and more pronounced growth of Co<sub>3</sub>O<sub>4</sub> during hydrothermal process in comparison to Cu<sub>2</sub>O, and so on. While increased presence of MOx may mean a larger presence of active sites for analyte interactions, it may decrease the conductivity of the sensing material, leading to higher base resistance. Additionally, Co<sub>3</sub>O<sub>4</sub> nanospheres are smaller than Cu<sub>2</sub>O nanospheres (figures 4.2.(c) and 4.2.(b) have the same magnification). This can further enhance the sensor sensitivity, as this would increase the surface-to-volume ratio. Finally, rGO/CuCoO<sub>x</sub> demonstrates the properties shown by both Cu<sub>2</sub>O and Co<sub>3</sub>O<sub>4</sub>, as expected. Both figures 4.2.(e) and 4.2.(f) show rGO flakes with MOx nanospheres which distinctively show a variation in their dimensions. This can be attributed to the coexistence of two types of metal oxides, copper and cobalt oxides in the structure. The material is therefore expected to possess characteristics of both nanocomposites.

#### 4.2.2 Rheology

Printability of the rGO/MOx synthesised ink is another important property that must be confirmed. This can be determined using a drop-watcher with sessile drop technique. The result of the analysis is provided in figure 4.3.

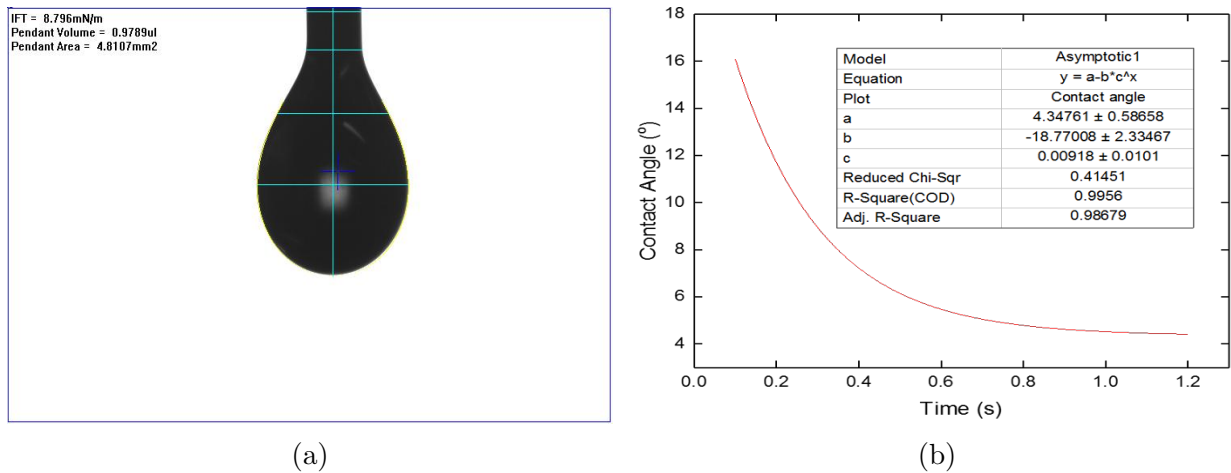


Figure 4.3: Rheology analysis performed on rGO/Co<sub>3</sub>O<sub>4</sub>

The sessile method drop consists of two parts. Firstly, the surface tension of the ink is obtained through pendant drop shape analysis. The shape of ink droplet suspended on a needle allows its geometry analysis to yield the surface tension value (see figure 4.3.(a)). The ink is then dropped on a Si/SiO<sub>2</sub> chip to calculate the contact angle values over time (see figure 4.3.(b)). Using these methods, it is observed that the rGO/Co<sub>3</sub>O<sub>4</sub> ink provides a surface tension of 8.796mN/m, which is within the preferable range for inkjet printing [43]. Additionally, the contact angle reached to about 4.5° in less than 1.5 seconds, displaying high wettability, thereby showing its adequacy for inkjet printing. The characterisation results for the two other inks, rGO/Cu<sub>2</sub>O and rGO/CuCoO<sub>x</sub> were not retrieved due to Covid-19.

### 4.3 Initial Gas Sensing Result

Once the ink characterisations are complete, it is possible to measure the sensor performance by exposing it to different analytes and environments. The gas sensor is locked in a sealed gas chamber connected to a computer, allowing users to record changes in resistance (measured using a Keithley digital multimeter connected to PC) as different gas cycles are introduced to the device (see figure 4.3).

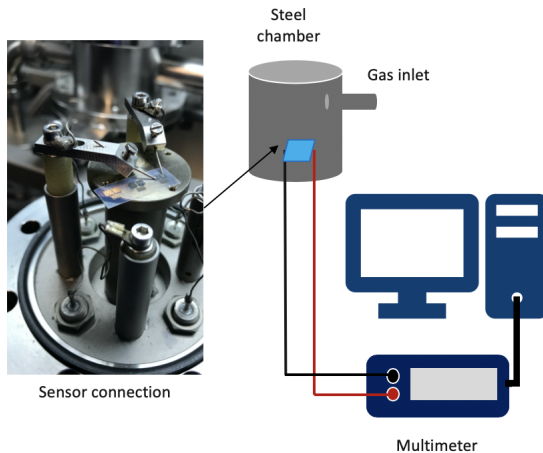


Figure 4.4: Gas sensor configuration with sensing instrument

The setup allows modifications in gas cycles (type of gas, duration of exposure, concentration and humidity settings) and the voltage applied throughout the measurements (DC mode or voltage sweep mode). This gives flexibility in the measurements. For the initial gas sensing experiments, rGO/Cu<sub>2</sub>O sensor is tested under the following conditions: 5 minutes exposure to varying concentrations of NO<sub>2</sub> from 100ppm to 20ppm with 10 minutes recovery period per exposure. This is expected to give the archetypal rGO/MO<sub>x</sub> response to an oxidising gas. The results are given with the S values plotted against time, and are shown below.

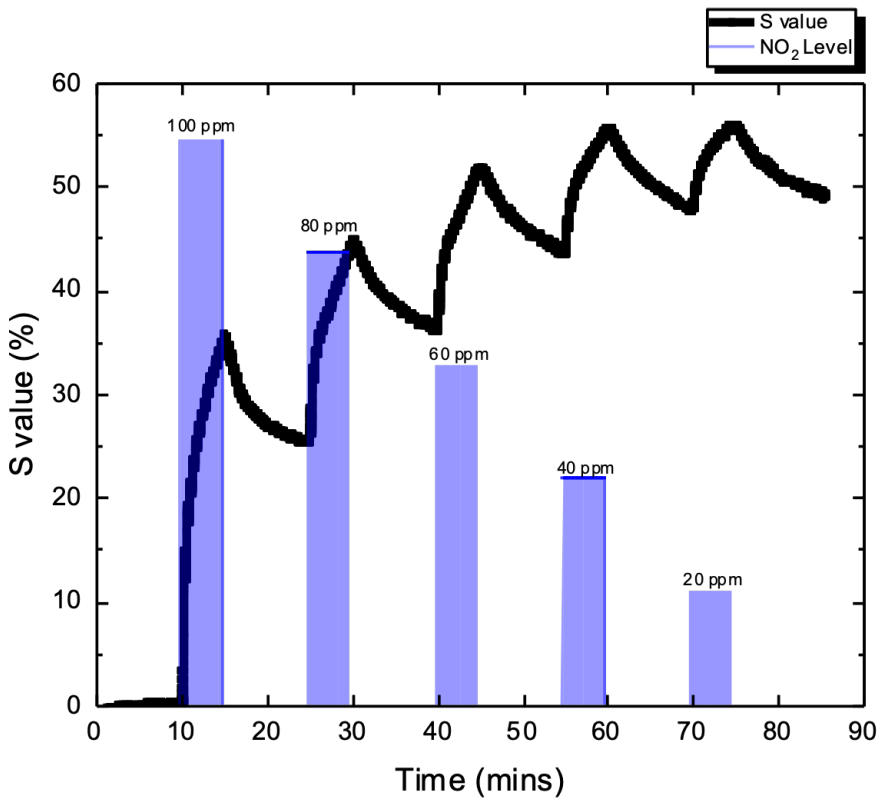


Figure 4.5: Gas sensor sensitivity against time with varying NO<sub>2</sub> concentrations

The graphical results show the sensor's reactions to the exposure to NO<sub>2</sub>. The S value increases exponentially following the exposure, which conforms with the theory: NO<sub>2</sub> is an oxidising gas, which increases carrier concentration in graphene upon exposure [7]. As the S value here is calculated using current, the line tends upwards (for S value calculated using resistance, increase in carrier concentration leads to a drop). The sensor result thus shows a correct response curve, similar to the one displayed in figure 2.6, with noticeable peaks and recovery during and after the periods of exposure. It is also important to note that the amplitude of the peaks are diminishing, due to decreasing NO<sub>2</sub> concentrations. Additionally, the curves show irreversibility of the responses from the presence of baseline drift. Indeed, due to the discrepancies in the response and recovery speed of the sensors, the curve shifts upwards with each exposure cycles. It can be noted that this trend weakens after each exposure, due to continued absorption of analytes by the devices, causing saturation to occur. The sensing result provided in figure 4.5, with the use of known material rGO/Cu<sub>2</sub>O, confirms the background theory detailed in the previous sections. The data will therefore act as the foundation of following experiments which tackle the two major issues of rGO/MOx based chemiresistive gas sensors: inaccuracies from baseline drift and poor selectivity.

# Chapter 5

## Sensor Optimisation - Baseline Drift

### 5.1 Background Theory

The initial gas sensing results confirm the theoretical background by displaying a baseline drift in the response curve. A strong emphasis can be placed this phenomenon, as it can be a source of significant error in the measurements. As observed from the graphs, the drift can cause a false prediction in ambient gas concentration, as even low concentrations can provide high response amplitude due to the drift. Several methods are being researched to fix this issue. The corrective measures so far are mostly concerned with application of signal processing algorithms to remove the baseline drift effect [44][45]. However, recent studies by Wu, T. revealed that application of heat pulses allows an improved sensor performance through significant reduction of baseline drift, via acceleration of recovery [41]. The use of pulses also improves energy efficiency of the system, in comparison to application of a level amount of heat. From this discovery, it was postulated that similar effects may be possible through application of current pulses. This can be corroborated by the equation for energy dissipation equation of a resistor as follows. Note that as the gas sensor used in the project is chemiresistive, the equation below will hold true for the component.

$$E = Pt = I^2Rt \quad (5.1)$$

This equation first indicates that Joule heating (self-heating of a circuit element,  $E$ ) is linearly proportional to the squared value of the current  $I$  flowing through it. Therefore, it was initially assumed that the resistance changes from analyte-sensing material reaction of the gas sensor is independent of the input current, and it was deemed that increasing the input current would lead to a rise in temperature as energy will be lost as heat. The equation then illustrates the power efficiency from using pulses. From an equal amount of energy provided,

it is possible to provide more or less power by controlling the time of the input  $I$ . Through modulation of the time of current supply, i.e. by using pulses, it is possible to reduce unnecessary power consumption in comparison to supplying level amount of current. Therefore, the input pulse is expected to provide similar effects as applying heat pulses, as energy dissipation in resistances leads to self-heating, providing thermal energy, while maintaining power efficiency. Overall, the experiment would in theory provide an improved sensor performance through baseline drift reduction via similar mechanism to that proposed by Wu, T.

It must be noted that the machine used for the experiment only allows modification in the applied voltage and is unable to input current directly onto the sensor. For this experiment, the input current modulation was therefore emulated using voltage modulations. The equation 5.1 can then be modified using Ohm's law. It was therefore deemed that the voltage input could replace the function of current input without contradicting the fundamental ideas behind the experiment. Thus by theory, a pulsing voltage will equivalently result in improved sensor performance through baseline drift reduction, while maintaining lower energy consumption. As the hypothesis created is valid for all rGO/MOx inks, only a single type of rGO/MOx, rGO/Co<sub>3</sub>O<sub>4</sub> was tested for convenience and ease of data comparison.

## 5.2 Pulse Exposure Results

To confirm baseline drift reduction with input voltage modulation, the experiment will be running the sensor under two modes of voltage modulation: DC step and V sweep. The DC step mode operates the gas sensor at a fixed voltage for a certain period of time, whereas V sweep mode enables voltage modulation by determining min/max values of voltage applied with the size of steps which determines the amplitude of voltage change per second. The limitations of both modes of operation are detailed in section 5.3.

For the experiment using DC step mode, rGO/Co<sub>3</sub>O<sub>4</sub> sensor was first put into saturation through repeated exposure to 100ppb NO<sub>2</sub> for 5 minutes, with recovery stages of 5 minutes after every exposure. The voltage across the sensor is kept at 1V during this process. The sensor becomes reasonably saturated, after about 6 cycles of exposure and recovery. New cycles are then introduced, where the recovery phase applies increased voltage of 2V, 4V, 6V, 8V, and eventually 10V (see figure 5.1, the red line marks the start of voltage increase). The exposure and recovery times are kept constant at 5 minutes. The result is then used to confirm whether an increase in voltage leads to accelerated recovery speed to allow baseline drift reduction.

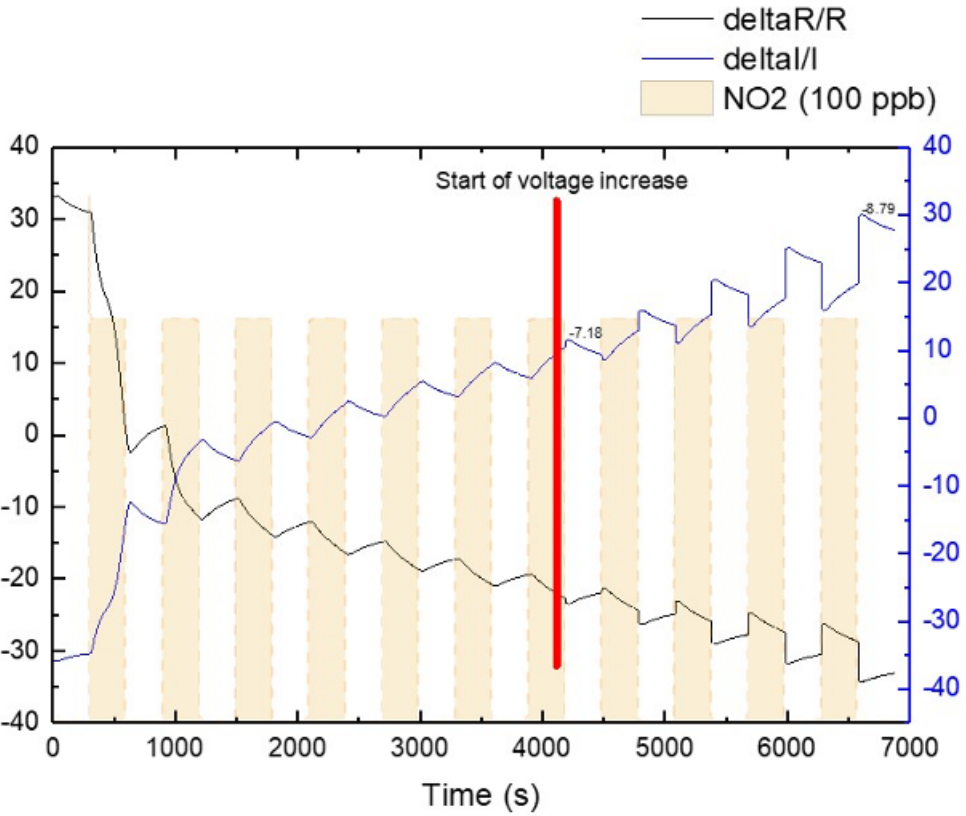


Figure 5.1: Effect of increasing voltage during recovery phase

The experiment using V sweep mode begins with DC voltage value (2V) used for all stages of gas sensing cycle until the recovery phase, where the gas sensing instrument then inputs a pulsing voltage signal. The concentration of  $\text{NO}_2$  during the exposure cycle is kept at 1ppm. Voltage sweep is then introduced for sensor recovery for 10 minutes. The amplitude of the sweep is varied throughout different experiments to determine its effect on sensor performance: for this report, voltage variations from 2-4V, 2-6V, and 2-8V, are selected. Once the first recovery cycle is complete, a second recovery cycle is introduced, where the DC voltage is set (back to 2V) for 10 minutes. To properly discern the effect of voltage sweep applied on the gas sensor, the S value is modified in the end to remove the sweep and connect the envelope (sweeping section) to the rest of the graph. This clearly provides the evolution of S value as sweeping voltage is introduced, and the drop in S value from its peak to its lowest value throughout recovery can be compared to discern the effect of voltage pulses to the sensor.

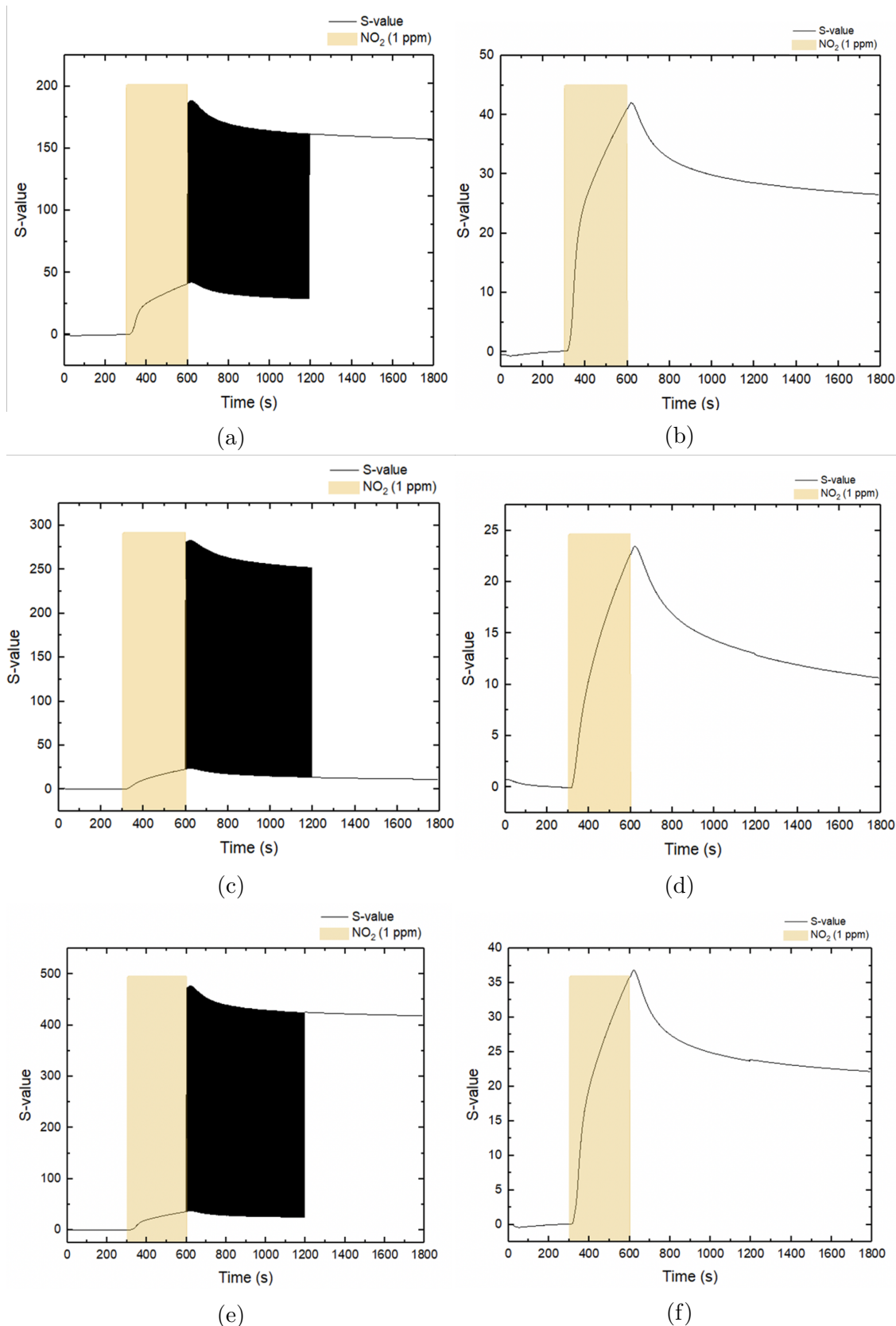


Figure 5.2: V sweep results with varying voltage sweep amplitudes (a)&(b) 2-4V, (c)&(d) 2-6V, and (e)&(f) 2-8V

### 5.3 Discussion

The first experiment provides both percentage changes in resistance and current as the gas sensor is exposed to different cycles. As explained previously, the exposure to NO<sub>2</sub> causes an increase in I (and thus decrease in R), which results in increasing values of  $\frac{\Delta I}{I}$  (and decreasing values of  $\frac{\Delta R}{R}$ ). As the DC voltage applied on the sensor increases, it is possible to note the increasing steepness of the recovery curve, where the gradient of the recovery evolves from -7.18 at 2V to -8.79 at 10V. This corresponds to a percentage change of around 22.4%, which can be deemed as low considering the voltage applied was quintupled. Additionally, there are unexpected instantaneous jumps of S value as increased voltages are introduced to the sensor (discussed later). Hence, the result from the first experiment corroborates the initial hypothesis, where the augmented voltage input result in higher desorption rate leading to an improved baseline recovery, as confirmed with increasing magnitude of recovery gradient. However, the rise in gradient value is a lot lower than expected, with a relatively small percentage change for a rise from 2-10V.

On the other hand, the second experiment using V sweep mode is unable to show the effect of voltage on the sensor. By observation of corrected S value plots in figure 5.2.(b) and figure 5.2.(f), it is confirmed that the fall in S value remains similar. 2-4V result show a S value drop of around 15% (41% to 26%), and 2-8V result show a comparable result of 14.5% (37% to 22.5%). The lack of disparity between the values despite significant increase in applied voltage indicates that the sweep had virtually no effect on the sensor's desorption speed, hence baseline drift reduction is unsuccessful. Moreover, from the 2<sup>nd</sup> recovery lines in figures 5.2.(a), (b), and (c) indicate that the gas sensing instrument is unable to correctly return to 2V DC value as instructed. The result's unreliability is further substantiated by figure 5.2.(d), which shows an unusually low maximum S value of about 24%. Overall, while the first experiment provided expected result by showing a correlation between recovery gradient and applied voltage, the second experiment was unable to demonstrate the effect of voltage pulses on baseline drift reduction.

The failure to achieve baseline drift reduction can be attributed to several reasons. First and foremost, the machine used for gas sensing is unable to input pulses that are suitable for the purpose of this experiment. The sensing instrument is in fact controlled by an access database, which only allows two modes of voltage input: DC or V sweep. The initial experiments were conducted using DC step mode, which was unable to provide control over voltage input in seconds. The minimum voltage cycle allowed by the machine was one minute, which

is too long to properly study the effect of pulsing input on sensor performance. On the other hand, while V sweep offers a faster input change with voltage variation every second, modification in its frequency is impossible. Moreover, the transition between the DC and V sweep presents a significant problem. As suggested in the previous paragraph, the machine is unable to bring the voltage level to what is fixed in the DC mode, but instead maintains arbitrarily the final value of V sweep stage (confirmed by other experiments involving such a transition).

Another significant problem can be identified once again with the gas sensing machine. The machine automatically returns error when working with higher voltage values, mainly due to Keithley multimeter's setting, which yields overflow error when working with current values outside its boundary. It is experimentally confirmed that increasing the voltage a slightly higher level leads to the device failure. This usually occurs at about 15V, which inhibits pulse testing as voltage value may be too low to trigger temperature increase from self-heating of the device.

Additionally, the core assumption when conducting this experiment is that the changes in sensor response would derive from the self-heating due to its energy dissipation. This is due to resistance being a material property independent of both I and V applied onto the device. However, the jumps in the sensor responses observed during input voltage changes seem to indicate a response dependence on an unknown factor, rather than temperature change from self heating. As shown from the figure, the sensitivity value of the sensor rises immediately after the change in input voltage. The absence of a delay indicates a discrepancy from a typical response caused by change of temperature.

The detailed mechanism behind this observed behavior isn't clearly known. However, it is possible to provide a few speculations. Studies by Mativetsky, J.M. reveal that voltage causes reduction of GO (graphene oxide), achieved with a relatively low voltage value of -3.6V [46] due to material instability. Therefore, the jumps in sensor response could have been caused by the increased voltage, inducing further reduction of rGO. This change in material property would lead to further increase in conductivity, as explained previously in section 4.1.1. The hypothesis seems to corroborate the experimental data, as increased voltage leads to an instantaneous upshoot in  $\frac{\Delta I}{I}$  (blue line on figure 5.1), and the opposite for  $\frac{\Delta R}{R}$  (black line on the same figure): both graphical results can be translated to an increase in sensor conductivity. This idea is reinforced by the amplitude of the sensor response increasing as larger voltages are applied. However, it must be noted that rGO, unlike GO, is an extremely stable material, and would require significant amount of voltage to cause a change in material

property. Moreover, by hydrothermal process's nature, which applies high heat and pressure over an extended period of time, it is highly probable that reduction of GO was fully achieved during the sensor synthesis stage. Therefore, additional reduction of rGO is very unlikely given its material property and the procedures involved in the experiment.

Overall, several elements hinder the proper experimental condition to be put in place. Due to several limitations, it was impossible to correctly test the effect of input I/V pulses onto gas sensor performance. Two possible solutions exist to avoid this issue. Firstly, another gas sensing instrument can be designed to provide the correct experimental condition. Another solution is to use software manipulation to modify the control system, to implement the desired environment. Additionally, the exact cause and mechanism behind the abnormal sensor behavior during voltage changes must also be clarified in future researches.

# Chapter 6

## Sensor Optimisation - Principal Component Analysis (PCA)

### 6.1 Background Theory - PCA

PCA corresponds to a data processing method which allows dimensionality reduction, as briefly described in section 2.2. In simple terms, the technique allows reduction of number of variables in a dataset while maintaining as much accuracy as possible, and the reduced number of variables allow simpler visualisation and further data analysis. In this section, the goal is to provide a step by step guidance of the technique, to help understand how it can be used to improve sensor performance in more depth. This part of the report also acts as a guide for the PCA code which is provided in the appendix A (pcafina.py).

PCA first begins by a process called standardisation. This is a data manipulation process in which the values in a dataset are transformed in order to have a mean of zero and a standard deviation of 1. This brings the values in a dataset to a comparable range, which ensures that one data point does not completely overshadow the other in terms of its importance, preventing the dataset to be biased. This is achieved through computation of z-score  $z_i$  of each value in a dataset, with equation 6.1.

$$z_i = \frac{x_i - \mu}{\sigma} \quad (6.1)$$

In this equation,  $x_i$  corresponds to a datapoint,  $\mu$  to the mean of the dataset, and  $\sigma$  to the standard deviation. This transformation stage thus allows all data points to be brought to the same scale. In the code provided in the appendix A (pcafina.py), this stage corresponds to line 42,  $X = StandardScaler().fit\_transform(Xoriginal)$ .

The following process in PCA corresponds to the calculation of the covariance matrix. Covariance corresponds to the measure of joint variability of two random variables [48]. The computation of covariance matrix therefore allows an understanding of correlation between different variables. For instance, for a 3-dimensional dataset with 3 variables, x, y, and z, the covariance matrix is a  $3 \times 3$  matrix of the following form.

$$\begin{pmatrix} Cov(x, x) & Cov(x, y) & Cov(x, z) \\ Cov(y, x) & Cov(y, y) & Cov(y, z) \\ Cov(z, x) & Cov(z, y) & Cov(z, z) \end{pmatrix}$$

$Cov(x,y)$  corresponds to the covariance of two variables x and y in the matrix above. Positive covariance value signifies that the variables are positively correlated, and negative covariance value signifies a negative correlation.

From the formation of the covariance matrix, it is now possible to obtain its eigenvalues and eigenvectors. Once the two are calculated, the eigenvalues are ordered in decreasing order. By doing so, it is possible to rank the principal components in terms of the amount of variance. The eigenvalue here corresponds to the amount of variance in the principal component, and its corresponding eigenvector describes the direction of the axis. In this step, dimensionality reduction is achieved by selecting the largest principal components. This leads to the formation of feature vectors, which are simply the eigenvectors with the highest eigenvalues selected for PCA [47].

Finally, once the previous steps are completed, it is possible to directly modify the dataset, and rearrange it to the axes determined by the selected principal components. This is achieved through the following operation.

$$Final\ data = Feature\ vector^T \times Modified\ data\ after\ standardisation^T \quad (6.2)$$

All the steps following the standardisation of the data can be achieved with line 45 and 48 of the code provided in the appendix A (pcafinal.py). The final form of dataset obtained from this operation can now be plotted as a scatter plot. This provides a comprehensive visual data by reorganising data. PCA applied on a data often forms visible clusters: for the application of gas sensors, a group of data would correspond to a sensor's response to a specific type of analyte. The technique therefore allows improved selectivity. Through such manipulation of data, it is possible to group and distinguish seemingly similar sensor responses to different analytes.

## 6.2 Background Theory - Classifiers

Once data manipulation is achieved from PCA, it is possible to enhance the selectivity through the use of classifiers. Classification corresponds to a technique in machine learning which assigns labels to datapoints based on known observations, called train set. This is a type of supervised learning, where learning occurs from known and correct instances. In broader terms, the technique is a type of pattern recognition algorithms, and several types of classifiers exist. The outcome of the classifiers are visualised as decision regions, each corresponding to different classes, on the scatter plot obtained from PCA

For this project, the classifiers used are logistic regression, Random Forest, Gaussian NB (naive Bayes), and SVM (support vector machine). While the models are all part of supervised learning models, which require input training data, they possess different mechanisms of learning and classifications. The models can be grouped as discriminative or generative models. Discriminative model includes logistic regression, Random Forest, and SVM. The output of this model is based on the predictions purely from input [49]. On the other hand, generative model includes Gaussian NB. The classification mechanism in the model is determined by not only the input variables, but also from variables based on outputs as well: the model generates all possible values for a phenomenon [49]. In terms of mathematics, the two models can be juxtaposed by the probabilities that are considered. Both models achieve classification by calculation of the posterior probability,  $P(y|x)$ , where  $x$  and  $y$  are the input and the output, respectively. While discriminative model achieves its calculation based on the parameters retrieved by  $x$ , the generative model makes use of joint probability of  $P(x,y)$ . The probabilities that are generated by the model through the consideration of the joint probability is then used to obtain the posterior probability using Bayes' theorem, which is given as the following equation [49][50].

$$P(y|x) = \frac{P(x|y)P(y)}{P(x)} \quad (6.3)$$

Naturally the discriminative model uses less variables for classifications, providing not only a faster classification output but also improved model accuracy, as they are more immune to overfitting and bias problems [49]. On the other hand, the generative model is more flexible, thanks to a better portrayal of the complex real-life system. Additionally, the generation of variables signifies comparable classification performance can be achieved to discriminative model using fewer input [50]. The four classifiers above are chosen to compare their performances by identifying the number of points outside their correct decision regions.

### 6.3 Application of PCA on Gas Sensing Data

With understanding on PCA and Classifiers, the different parameters and settings involved in PCA can be explained. Firstly, three parameters are chosen for PCA to be reduced are: maximum S value, area ratio, and response time. All three parameters can be retrieved from raw data provided by the gas sensing instrument: maximum S is the percentage change of sensor I at its peak, area ratio is the calculated from response area/recovery area, and response time is the time taken between reaching from 10% to 90% of the maximum value. The dimensionality is then reduced from 3D to 2D by choosing two principal components. The three parameters are chosen due to their excellence in characterising gas sensing behavior: maximum S determines the strength of the response, area ratio describes sensor response's reproducibility, and response time shows the sensor responsiveness.

The three parameters can also be compared qualitatively in terms of their importance to PCA results. Through variance values of the principal components, it is possible to determine which parameter is the most significant. This can be achieved by comparing how randomness of each parameter affects the variance of the principal components. To achieve this, pseudo-random data is created (code provided in appendix A, randomgen.py), using normal distribution where the mean is the real data and the standard deviation ( $\sigma$ ) is user-defined. Single  $\sigma$  value is used, determined using CV (coefficient of variation). CV is the ratio between  $\sigma$  and mean of the data, and is set to 0.5 for the parameter of interest while others are kept at 0.01.

Parameter	PC1	PC2
<b>Max S</b>	75.58%	13.41%
<b>Response T</b>	51.72%	33.34%
<b>A Ratio</b>	75.66%	15.55%

Table 6.1: Variation of PCs from parameter randomness

The table above displays the changes in PCs from equal degree of randomness introduced to the data. From the result, it can be judged that the parameter which affects the data the most is the response time, followed by maximum S, and area ratio.

Finally, 4 classifiers are chosen as mentioned above, with 3 discriminative models and one generative model. More discriminative models were chosen as they are considered to be more favorable as classifiers, as explained previously. Within the discriminative models,

there are clear differences in their nature: logistic regression is a linear model forming linear decision regions, Random Forest is a model based on decision trees, and finally SVM is set to exponential mode to allow non-linear differentiation of data. The settings for the classifiers are set to default settings to capture their typical classifying ability.

## 6.4 PCA Results

To confirm whether selectivity can be improved using PCA, rGO/CuCoO<sub>x</sub> sensor is tested on a mixed gas of NO<sub>2</sub> and NH<sub>3</sub>, both with a concentration of 200ppb, at a dry condition and at a wet condition with humidity of 10%. It is also tested on wet air with 10% humidity. The sensor is unsaturated for all experiments for uniformity. Once all necessary data is prepared, PCA with the four classifiers is applied to rGO/CuCoO<sub>x</sub> sensor's responses to the mixed gas in dry and humid (10% humidity) conditions, and to 10% humidity, to test its ability to distinguish between different analytes. Then, the technique is applied for mixed gas in different humidity values, 0%, 10%, 20%, and 30%. Results are visualised as scatter plots with 4 different classifiers.

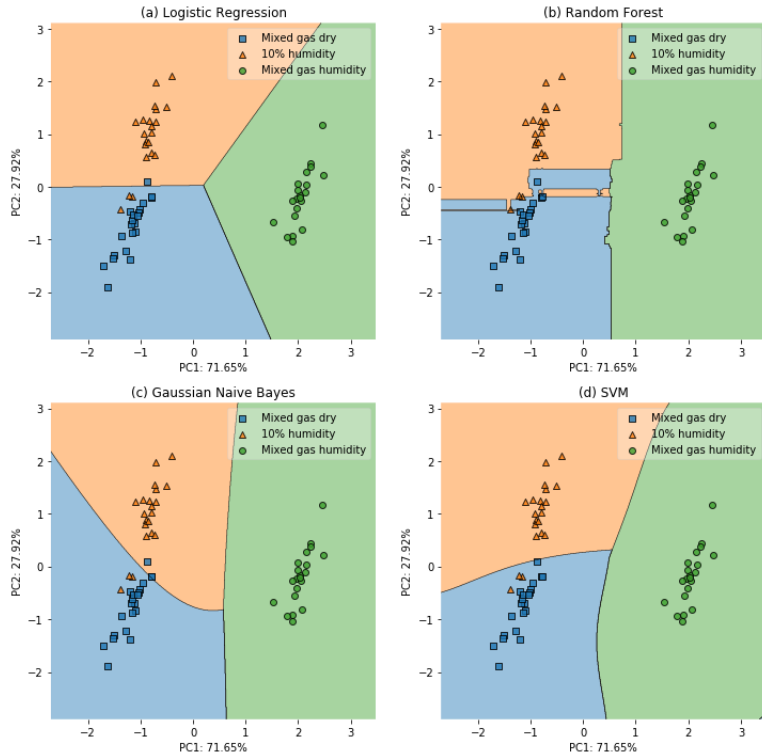


Figure 6.1: rGO/CuCoO<sub>x</sub> response to mixed gas in dry and in 10% humidity condition (marked as Mixed gas dry and Mixed gas humidity, respectively), and wet air with 10% humidity (marked as 10% humidity),  $\sigma=2.2$

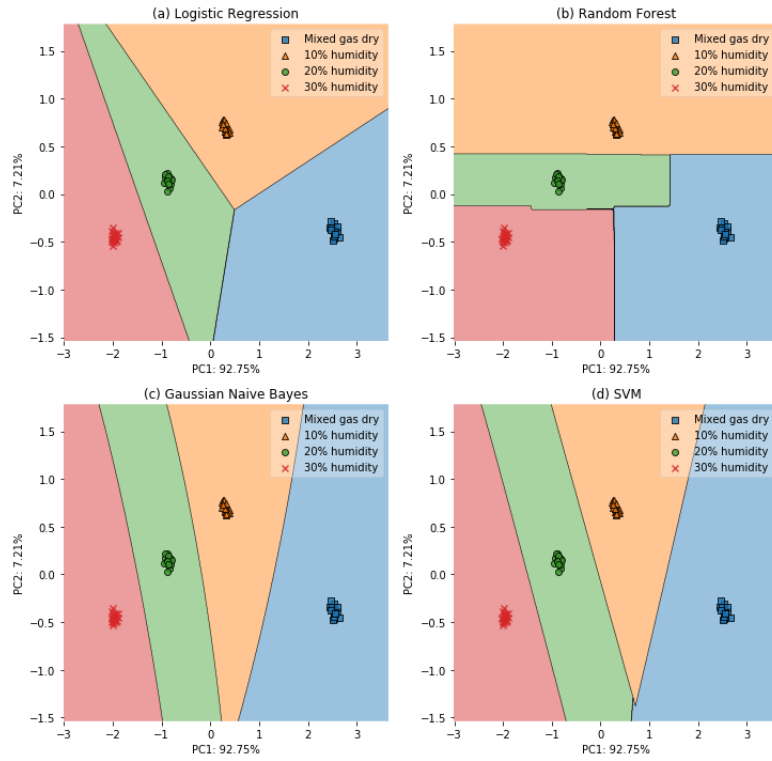


Figure 6.2: rGO/CuCoO<sub>x</sub> response to mixed gas in 4 different humidity settings, CV = 0.01

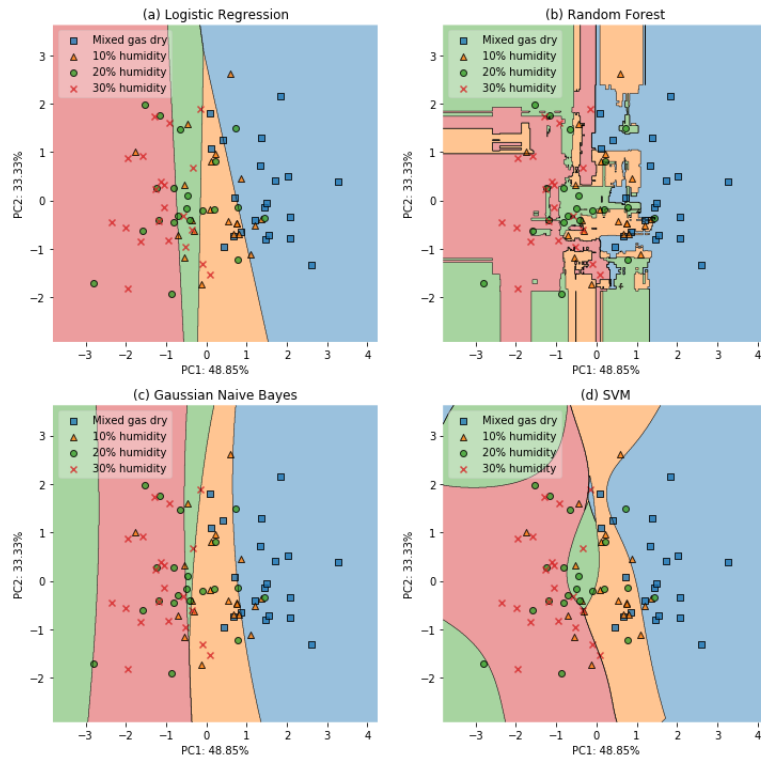


Figure 6.3: rGO/CuCoO<sub>x</sub> response to mixed gas in 4 different humidity settings, CV = 0.5

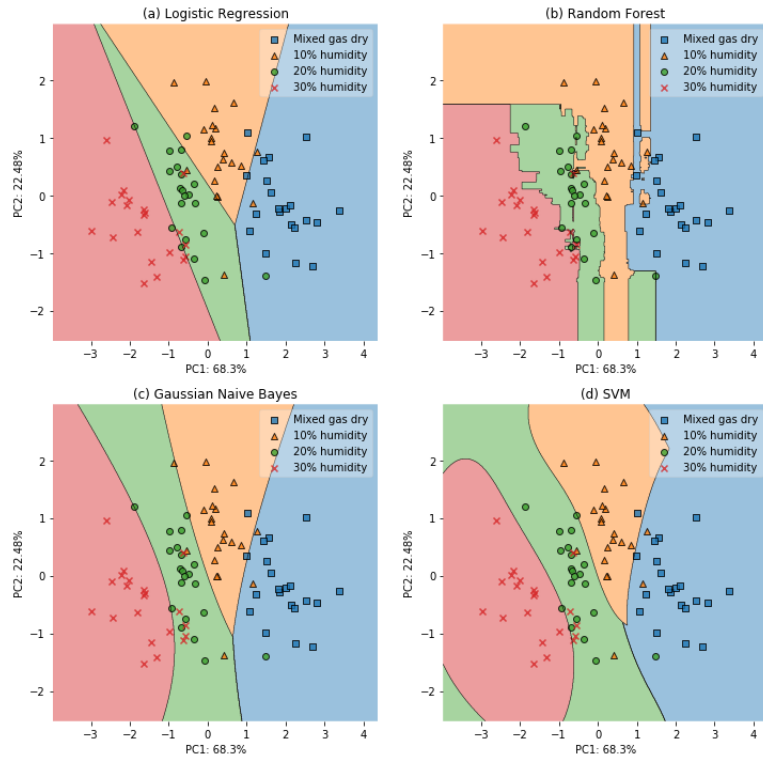


Figure 6.4: rGO/CuCoO<sub>x</sub> response to mixed gas in 4 different humidity settings,  $\sigma=2.2$

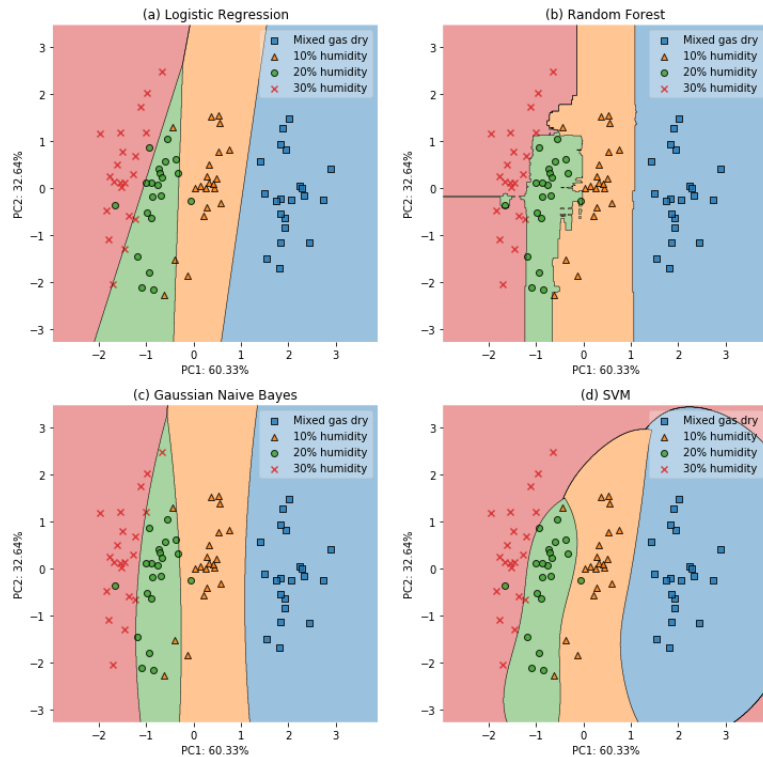


Figure 6.5: rGO/CuCoO<sub>x</sub> response to mixed gas in 4 different humidity settings, CV = 0.15

Due to Covid-19, it was impossible to obtain significant amount of data on this experiment: the test described above was done once, and only 10% humidity was tested by another lab member. To circumvent the lack of data, approximate values for mixed gas response in humidity of 20% and 30% are generated using both linear and exponential approximation based on real values of 0% and 10% humidity. In all figures, pseudo-random data is created in the same was as described in the previous section. Different  $\sigma$  values are experimented in terms of CV. Additionally,  $\sigma$  of 2.2 is used for figure 6.1 and 6.4, corresponding to  $\sigma$  in typical rGO/MOx response, obtained by previous researches in the group.

## 6.5 Discussion

The first PCA result seen in figure 6.1 shows rGO/CuCoO<sub>x</sub> response to three different analytes using  $\sigma$  of 2.2: by using  $\sigma$  obtained from experimental data, it is possible to portray possible experimental outcome. It can be seen that all four classifiers successfully created distinguishable decision regions with acceptable level of accuracy. It can also be observed that 3 points from 10% humidity class are located in the wrong decision region, mixed gas humidity. However, they can be discarded as they can be judged as outliers produced from pseudo-random generator. The scatter plot thus shows a positive result, as it was able to correctly identify the sensor responses to the analytes.

The four following PCA results from figure 6.2. to figure 6.5 are then obtained by testing rGO/CuCoO<sub>x</sub> to mixed NO<sub>2</sub> & NH<sub>3</sub> gas in four different humidity conditions, with varying standard derivation settings used during pseudo-random data generation. The comparison of these figures display the effect of modifying CV on the sensor's selectivity performance. This is made explicit through juxtaposition of figures 6.2 and 6.3. Figure 6.2 uses an extremely small derivation at 1% of data mean value, resulting in a narrow dispersion of datapoints in the scatter plot. This thereby facilitates the classifier to define accurate boundary regions with no datapoints outside their corresponding decision regions. In contrast, figure 6.3 uses a much larger  $\sigma$  value, leading to a significant increase in data dispersion. The datapoints' location is much more random, leading to very imprecise decision regions. It is also observable that the increase in CV causes the variance of PC1 to diminish and PC2 to increment: this signifies that the data is no longer organised on the first principal component to tend towards randomness, which is to be expected from an increase in  $\sigma$ .

Figure 6.4 displays the predicted sensor result, through the use of experimentally obtained  $\sigma$  value. The result on the scatter plot shows a fairly positive outcome, with 5 incorrect

datapoints on average per class. This signifies that the rGO/CuCoO<sub>x</sub> sensor would be able to correctly determine the analyte with an approximate accuracy of 75%. On the other hand, figure 6.5 uses CV value of 0.15, which was experimentally found to be the largest CV value providing an acceptable accuracy. The result show approximately 1 to 1.5 incorrect points per class, leading to an approximate accuracy of 95%.

While the use of classifiers on PCA can be used to determine the selectivity performance of rGO/CuCoO<sub>x</sub> gas sensor, its results can also be exploited to evaluate the sensor synthesis process. Through repeated measurements, it is possible to obtain the  $\sigma$  values for each sensor parameter used for PCA. The calculated  $\sigma$  can then be used pseudo-random generator, to plot the data in PCA and predict the classifier behavior. The result can therefore be analysed, and the varying presence of datapoints outside their correct decision regions will indicate the quality of the sensor manufacturing process.

Additionally, the results from the experiments allow the evaluation of the different classification models used and confirm the theory in section 6.3. The performance of each classifiers can be analysed by comparing the total number of incorrect datapoints. This can be used to determine which classifier provides the highest performance in terms of accuracy.

<b>Figure</b>	<b>Logistic Regression</b>	<b>Random Forest</b>	<b>Gaussian NB</b>	<b>SVM</b>
<b>6.1</b>	4	0	4	3
<b>6.2</b>	0	0	0	0
<b>6.3</b>	41	0	38	34
<b>6.4</b>	14	0	13	12
<b>6.5</b>	6	0	6	4

Table 6.2: Total number of incorrect points per classifier in 5 scatter plots

From the first look at the table, it may seem that the Random Forest classifier provides the most accurate results, with 0 incorrect datapoint for all figures. However, the table falsely reports the classifier performance. Random Forest is a model based on decision tree, which often leads to overfitting of the data. Decision trees often do not consider the particularity of the data, which results in the model becoming "granular": this means that the model will learn even from outlier datapoints, resulting in overfitting. At first, overfitting may seem beneficial as this may reduce error to 0 during learning as seen in the table. However, the data will present significant inaccuracies when introduced to novel data inputs, and will have poor prediction accuracy. While Random Forest is an enhanced model which averages

different decision trees to prevent learning from irregular patterns, overfitting nevertheless occurred due to the small number of data, which reduces the averaging effect of Random Forests [51].

On the other hand, the three other classifiers show similar degrees of errors. Logistic regression model is found to be the least accurate, mainly due to the model being linear, which naturally leads to inaccuracies. This leaves two suitable models, Gaussian NB and SVM. While both models are robust against overfitting, with non-linear decision regions, SVM presents a slight advantage in terms of the model accuracy with slightly lower number of incorrect data points. The cause of the difference can be attributed to the distinction between generative (Gaussian NB) and discriminative model (SVM). As described earlier, the discriminative model is the more suitable option for data classification. The results thus substantiate the theory as SVM presents better accuracy over Gaussian NB. Therefore, it can be concluded that the optimal classifier for gas sensing analytes, from data obtained using pseudo-random generators, is SVM. However, it can be argued that Gaussian NB may be more suitable if real data were used, as generative models perform better with real life data due to the model complexity.

Finally, modification in the PCA software can be made for users to predict the type of unknown gas detected by the sensor. The software provided in the appendix A allows an additional function, where user is able to input the three parameter values. The values are then processed using PCA and a new datapoint is marked on the scatter plot as a black dot. An example of such user input is provided in appendix A (`user_input.png`).

Overall, the results successfully visualised PCA technique's capability of distinguishing different analytes, improving device selectivity. While it is confirmed that the optimisation is successful on the pseudo-random data, the test must be run on real data that will be taken once the university is functional. Additionally, it must be noted that the positive result may also be attributed to this lack of data: the values for 20% and 30% derived purely from approximations based on the existing values, and were therefore distinct. In real life scenario, it is possible that the values are much harder to distinguish, resulting in a more difficult environment for a successful PCA.

# Chapter 7

## Conclusion

### 7.1 Main Findings

Through this project, I was able to identify different characteristics of the rGO/MOx sensors identify two key issues which required improvement: the presence of baseline drift and selectivity issues. The suggested methods to address the two issues were: operation of gas sensor using input pulses for baseline drift reduction and data processing using PCA for improved selectivity. Cu<sub>2</sub>O, Co<sub>3</sub>O<sub>4</sub>, and CuCoO<sub>x</sub> were used as MOx to be incorporated into rGO. Each rGO/MOx sensor was used to deepen the understanding on the nanocomposite based gas sensors, and to optimise sensor performance through the methods above. While baseline drift reduction through pulse input was unsuccessful due to various reasons, selectivity improvement using PCA saw positive outcomes which allowed successful distinction between analytes.

### 7.2 Ideas for the future

Firstly, the major improvements can be made in baseline drift reduction. The main source of failure was the limitations from gas sensing instrument, which can be solved either by using another equipment or by modifying the software controlling the machine. Further research will be also required in understanding the material behavior, which will help clarify whether baseline drift reduction is possible using the method suggested in this report. On the other hand, PCA results were positive, with analytes classification achieved, several points of improvement exist. The technique must be tested on real data, which can be retrieved once the university is functional. Finally, PCA can be made more elaborate by applying more than 3 existing parameters, and more classifiers can be tested to yield the best results.

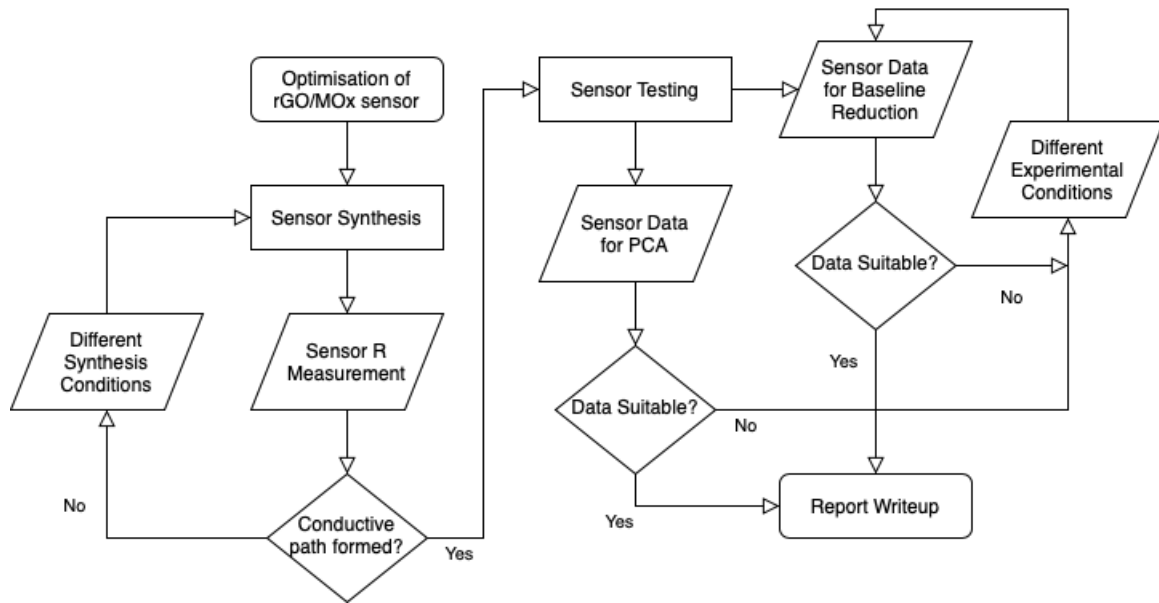


Figure 7.1: Workflow for the IIB project

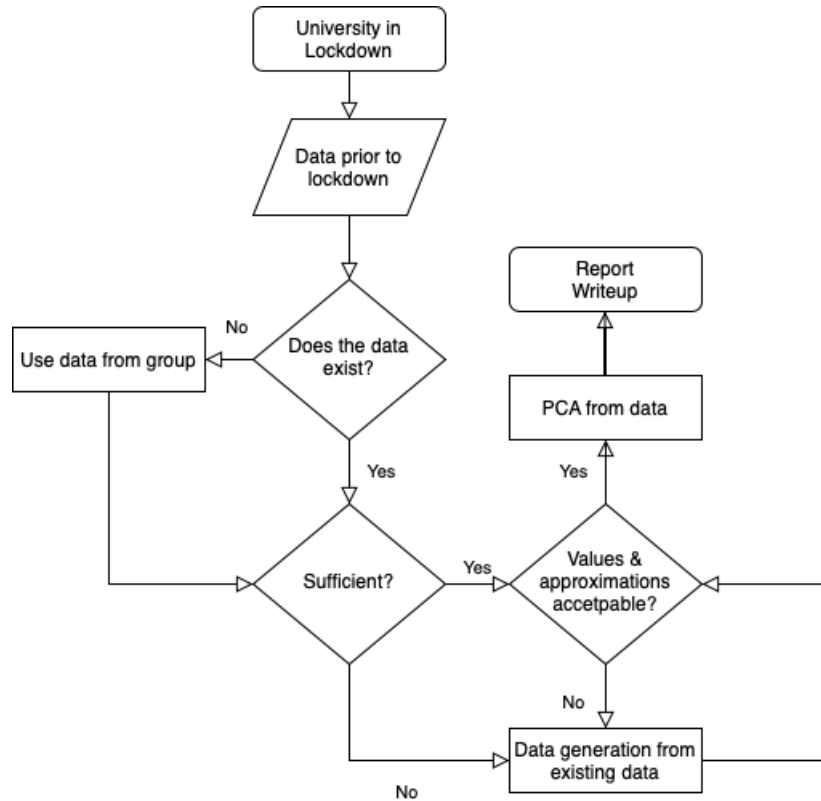


Figure 7.2: Workflow for the IIB project during easter term due to Covid-19

# Bibliography

- [1] London: Longman; Brown; Green; & Longmans. **The Report of the South Shields Committee, appointed to investigate the cause of Accidents in Coal Mines.** 1843.
- [2] Janata, J.; Bezegh, A. **Chemical Sensors.** *Anal. Chem.* vol. 60, pp. 62-74, 1988.
- [3] Bănică, F.G. **Chemical Sensors and Biosensors: Fundamentals and Applications.** 2012.
- [4] Chou, T.; et al. **Chemical, Gas, and Biosensors for Internet of Things and Related Applications.** chp. 16, pp. 237-252, 2019.
- [5] Sun, Y.F.; et al. **Metal Oxide Nanostructures and Their Gas Sensing Properties: A Review.** *Sensors.* vol.12, no.3, pp. 2610-2631, 2012.
- [6] Pijolat, C. **Chemical Sensors and Biosensors.** *John Wiley & Sons.* pp. 93-125, 2013.
- [7] Meng, Z.; et al. **Electrically-Transduced Chemical Sensors Based on Two-Dimensional Nanomaterials.** *Chem. Rev.* vol. 119, pp. 478-598, 2019.
- [8] Rao, C.N.; et al. **Graphene: The New Two-Dimensional Nanomaterial.** *Angew. Chem., Int. Ed.* vol. 48, pp. 7752-7777, 2009.
- [9] Sun, Y.; et al. **Atomically Thin Tin Dioxide Sheets for Efficient Catalytic Oxidation of Carbon Monoxide.** *Angew. Chem., Int. Ed.* vol. 52, pp. 10569-10572, 2013.
- [10] Xia, F.; et al. **Two-Dimensional Material Nanophotonics.** *Nat. Photonics.* vol. 8, pp. 899-907, 2014.
- [11] Sehkar, P.K.; et al. **Chemical Sensors for Environmental Monitoring and Homeland Security.** *Electrochem. Soc. Interface.* vol. 19, pp. 35-40, 2010.
- [12] Paolesse, R.; et al. **Porphyrinoids for Chemical Sensor Applications.** *Chem. Rev.* vol. 117, pp. 2517-2583, 2017.

- [13] Zeghbroeck, V. **Principles of Semiconductor Devices and Heterojunctions.** *Prentice Hall PTR.* 2007.
- [14] Neamen, D. **An Introduction to Semiconductor Devices.** *McGraw-Hill, Inc.: New York.* pp. 720, 2006.
- [15] Kahn, A. **Fermi Level, Work Function and Vacuum Level.** *Mater. Horiz.* vol. 3, pp. 7-10, 2016.
- [16] Tung, R.T. **The Physics and Chemistry of the Schottky Barrier Height.** *Appl. Phys. Rev.* vol. 1, 011304, 2014.
- [17] Griffiths, D.J. **Introduction to Electrodynamics.** *Cambridge University Press: Cambridge.* 2017.
- [18] Blackwood, D.; Josowicz, M. **Work Function and Spectroscopic Studies of Interactions between Conducting Polymers and Organic Vapors.** *J. Phys. Chem.* vol. 95, pp. 493-502, 1991.
- [19] Pinto, H.; Markevich, A. **Electronic and Electrochemical Doping of Graphene by Surface Absorbates.** *Beilstein J. Nanotechnol.* vol. 5, pp. 1842-1848, 2014.
- [20] Liu, B.; et al. **High-Performance Chemical Sensing Using Schottky-Contacted Chemical Vapor Deposition Grown Monolayer MoS<sub>2</sub> Transistors.** *ACS Nano* vol. 8, pp. 5304-5314, 2014.
- [21] Ruths, P.F.; et al. **A Study of Pd/Si MIS Schottky Barrier Diode Hydrogen Detector.** *IEEE Trans. Electron Devices.* vol. 28, pp. 1003-1009, 1981.
- [22] Sharma, B.L. **Metal-Semiconductor Schottky Barrier Junctions and Their Applications.** *Springer, Boston, MA.* 1984.
- [23] Fonash, S.J.; et al. **Conducting MIS Diode Gas Detectors: The Pd/SiO<sub>x</sub>/Si Hydrogen Sensor.** *Sens. Actuators.* vol. 2, pp. 363-369, 1981.
- [24] Barsan, N.; Weimar, U. **Conduction Model of Metal Oxide Gas Sensors.** *J. Electroceram.* vol. 7, pp. 143-167, 2001.
- [25] Potje-Kamloth, K. **Semiconductor Junction Gas Sensors.** *Chem. Rev.* vol. 108, pp. 367-399, 2008.

- [26] Romain, A.C.; Nicolas, J. **Long Term Stability of Metal Oxide-Based Gas Sensors for e-Nose Environmental Applications: An Overview.** *Sens. Actuators*. vol. 146, 9 pp. 502-506, 2010.
- [27] Sisk, B.C.; Lewis, N.S. **Comparison of Analytical Methods and Calibration Methods for Correction of Detector Response Drift in Arrays of Carbon Black-Polymer Composite Vapor Detectors.** *Sens. Actuators, B*. vol. 104, pp. 249-268, 2005.
- [28] Harris, D.C. **Quantitative Chemical Analysis.** *W.H. Freeman*. 2016.
- [29] Li, P.; et al. **Ultra-Sensitive Suspended Atomically Thin-Layered Black Phosphorus Mercury Sensors.** *Biosens. Bioelectron*. vol. 98, pp. 68-75, 2017.
- [30] Chandran, G.T.; et al. **Electrically Transduced Sensors Based on Nanomaterials (2012-2016).** *Anal. Chem.* vol. 89, pp. 249-275, 2017.
- [31] Korotcenkov, G.; Cho, B.K. **Metal Oxide Composites in Conductometric Gas Sensors: Achievements and Challenges.** *Sensors and Actuators B: Chemical*. vol. 244, pp. 182-210, 2017.
- [32] Fennell, J.F., Jr.; et al. **Nanowire Chemical/Biological Sensors: Status and a Roadmap for the Future.** *Angew. Chem., Int. Ed.* vol. 55, pp. 1266-1281, 2016.
- [33] Jolliffe I.T. **Principal Component Analysis.** *Springer Series in Statistics, 2nd ed.* p. 28, 2002.
- [34] Nallon, E.C.; et al. **Chemical Discrimination with an Unmodified Graphene Chemical Sensor.** *ACS Sens.*, vol. 1, pp. 26-31, 2016.
- [35] Ponzoni, A.; et al. **Metal Oxide Gas Sensors, a Survey of Selectivity Issues Addressed at the SENSOR Lab, Bresica (Italy).** *Sensors (Basel)*. vol. 17(4), pp. 714, 2017.
- [36] Sarf, F. **Metal Oxide Gas Sensors by Nanostructures.** 2019.
- [37] Yuan, Z.; et al. **Approaches to Enhancing Gas Sensing Properties: A Review** *Sensors (Basel)*. vol. 19(7), pp. 1495, 2019.
- [38] Mohan, V.B.; et al. **Characterisation of Reduced Graphene Oxide: Effects of Reduction Variables on Electrical Conductivity.** *Materials Science and Engineering: B*. vol. 193, pp. 49-60, 2015.

- [39] Yin, P.T.; et al. Design, Synthesis and Characterization of Graphene-Nanoparticle Hybrid Materials for Bioapplications. *Chem. Rev.* vol. 115, pp. 2483-2531, 2011.
- [40] Deng S.; et al. Reduced Graphene Oxide Conjugated Cu<sub>2</sub>O Nanowire Mesocrystals for High-Performance NO<sub>2</sub> Gas Sensor. *J. Am. Chem. Soc.* vol. 134, pp. 4905-4917, 2012.
- [41] Wu, T.; et al. Inkjet-printed CMOS-integrated Graphene–metal Oxide Sensors for Breath Analysis *npj 2D Mater Appl.* vol.3, pp. 42, 2019.
- [42] Mazlan, N.S.; et al. Interdigitated Electrodes as Impedance and Capacitance Biosensors: A Review *AIP Conference Proceedings*. 2017.
- [43] Carey, T.; et al. Fully Inkjet-Printed Two-Dimensional Material Field-Effect Heterojunctions for Wearable and Textile Electronics. *Nat. Commun.* vol.8, p. 1202, 2017.
- [44] Jiang, P.; Zhu, R. Elimination of Drifts in Long-Duration Monitoring for Apnea-Hypopnea of Human Respiration. *Sensors (Basel)*. vol. 16, pp. 1779, 2016.
- [45] Wilson, J.D.; et al. The Elimination of Errors due to Baseline Drift in the Measurement of Peak Areas in Gas Chromatography. *Journal of Chromatography A*. vol. 19, pp. 486-494, 1965.
- [46] Mativetsky, J.M.; et al. Local Current Mapping and Patterning of Reduced Graphene Oxide. *J. Am. Chem. Soc.* vol. 132, pp. 14130-14136, 2010.
- [47] Rice, J. Mathematical Statistics and Data Analysis. *Belmont, CA*. pp. 138, 2017.
- [48] Smith, L.I. A tutorial on Principal Components Analysis. 2002.
- [49] Ulusoy, I.; Bishop, C.M.; Comparison of Generative and Discriminative Techniques for Object Detection and Classification. *Microsoft Research, Cambridge*. 2016.
- [50] Nguyen, A.Y.; et al. On Discriminative vs. Generative Classifiers: A Comparison of Logistic Regression and Naive Bayes. *Adv. Neural Inf. Process Sys.* 2. 2002.
- [51] Friedman, J.H.; et al. The Elements of Statistical Learning. 2001.

# Appendix A

## Codes for PCA/Classifiers and Pseudo-Random Data Generator

The link provides the codes used for the project, please click the following to access the codes:  
<https://drive.google.com/drive/folders/128kPot2ps0QnoRkVby2TbdjepV4ahn6W?usp=sharing>

pcafina.py corresponds to the code containing PCA/classifiers, and randomgen.py corresponds to the code containing the pseudo-random data generator. A .csv file is also included to allow the code to be tested. Please run randomgen.py first to generate datapoints, then run pcafina.py to show them on the scatter plot. user\_input.png image shows an example of user input feature added to the pcafina.py code.

## **Appendix B**

### **Risk Assessment Retrospective**

Two risks identified in the beginning of the project: presence of hazardous substances (graphene flakes) and gases (fully contained in a vacuum system). Both had their risk assessment completed. The assessment well reflected the hazards which were present during the project, as I went through both sensor synthesis process involving GO power and gas sensing using a dedicated instrument. In retrospect however, I would like to add a physical risk: the gas sensing instrument, if kept untidy, contains sharp pieces of glasses from broken samples.

# Appendix C

## Covid-19 Disruption

Originally, several gas sensor measurements were expected to take place during Easter vacation. This mainly includes measurements of analytes in different humidity conditions which would be used to provide data for PCA, as well as several characterisation tests which all require use of laboratory equipment. The planned activities that were disrupted are as follows.

- Measurement of rGO/Co<sub>3</sub>O<sub>4</sub> and rGO/CuCoO<sub>x</sub> response to analytes in different humidity conditions (only rGO/CuCoO<sub>x</sub> data used, with a single iteration of the experiment).
- Novel SEM images for report for the three types of MOx (images from previous SEM sessions used in this report).
- RAMAN/UV visible spectroscopy for the three types of MOx
- Rheology measurements (drop watcher) for the three types of MOx, only rGO/Co<sub>3</sub>O<sub>4</sub> used for the report.

Due to the university lockdown, it was impossible to access the lab equipment required to undergo these tests. The only option was to use data from the lab group with a pseudo-random data generator, which significantly decreases my data credibility. Additionally, as the data had only one iteration for a single sensor type, rGO/CuCoO<sub>x</sub>, the accuracy of the results is further discredited. Finally, the work environment was far from ideal, due to several factors such as being quarantined as a returnee from overseas. Overall, several significant disruptions were caused from Covid-19, preventing me from producing optimal outcome for the project.